

Contents lists available at ScienceDirect

Applied Mathematical Modelling

journal homepage: www.elsevier.com/locate/apm



Modelling and direct numerical simulation of flow and solute dispersion in the spinal subarachnoid space



C. Gutiérrez-Montes ^{a,f,*}, W. Coenen ^b, J.J. Lawrence ^c, C. Martínez-Bazán ^{a,d,f}, A.L. Sánchez ^c, J.C. Lasheras ^{c,e}

- ^a Área de Mecánica de Fluidos, Departamento de Ingeniería Mecánica y Minera, Universidad de Jaén, Campus de las Lagunillas, Jaén 23071, Spain
- ^b Grupo de Mecánica de Fluidos, Departamento de Ingeniería Térmica y de Fluidos, Universidad Carlos III de Madrid, Leganés 28911, Spain
- ^c Department of Mechanical and Aerospace Engineering, University of California San Diego, USA
- ^d Área de Mecánica de Fluidos, Departamento de Mecánica de Estructuras e Ingeniería Hidráulica, Universidad de Granada, Campus Fuentenueva s/n, Granada, 18071, Spain
- ^e Department of Bioengineering, University of California San Diego, USA
- ^fAndalusian Institute for Earth System Research, Universidad de Jaén, Campus de las Lagunillas, Jaén, 23071, Spain

ARTICLE INFO

Article history: Received 29 April 2020 Revised 19 January 2021 Accepted 24 January 2021 Available online 30 January 2021

This paper can be classified under: Computational fluid dynamics Spinal CSF flow Solute transport Analytical modelling

Keywords: Cerebrospinal fluid Spinal canal Intrathecal drug delivery

ABSTRACT

The motion of the cerebrospinal fluid in the spinal subarachnoid space, a slender annular canal surrounding the spinal cord, exhibits an oscillatory velocity component driven by the pressure oscillations induced by the cardiac and respiratory cycles. A time-averaged transport equation has been recently proposed for describing solute transport along the canal, circumventing the need to compute the concentration fluctuations resulting from this fast oscillatory motion. The accuracy and limitations of this time-averaged description are tested here by means of comparisons with results of direct numerical simulations spanning hundreds of oscillation cycles, as needed to generate significant dispersion of the solute. The comparisons between the numerical results and the predictions of the analytical model include velocity fields and quantifications of transient solute-dispersion events for selected values of the flow parameters and two different idealized, canonical geometries of the spinal canal. The comparisons clearly demonstrate the accuracy of the timeaveraged description of the analytical model, which is seen to provide a good fidelity at a fraction of the computational cost involved in the direct numerical simulations. The variations of canal eccentricity along the spinal canal are found to play an important role in the dynamics of the solute transport, leading to the emergence of closed recirculating Lagrangian vortices that may hinder solute dispersion along the canal, as revealed by both direct numerical simulations and time-averaged results.

© 2021 Elsevier Inc. All rights reserved.

1. Introduction

The cerebrospinal fluid (CSF) is a clear fluid with water-like properties (i.e. density $\rho \simeq 10^3$ kg/m³ and kinematic viscosity $\nu = 0.7 \times 10^{-6}$ m²/s) that bathes the central nervous system (CNS). Its motion, generated by the quasi-periodic pressure

E-mail address: cgmontes@ujaen.es (C. Gutiérrez-Montes).

^{*} Corresponding author.

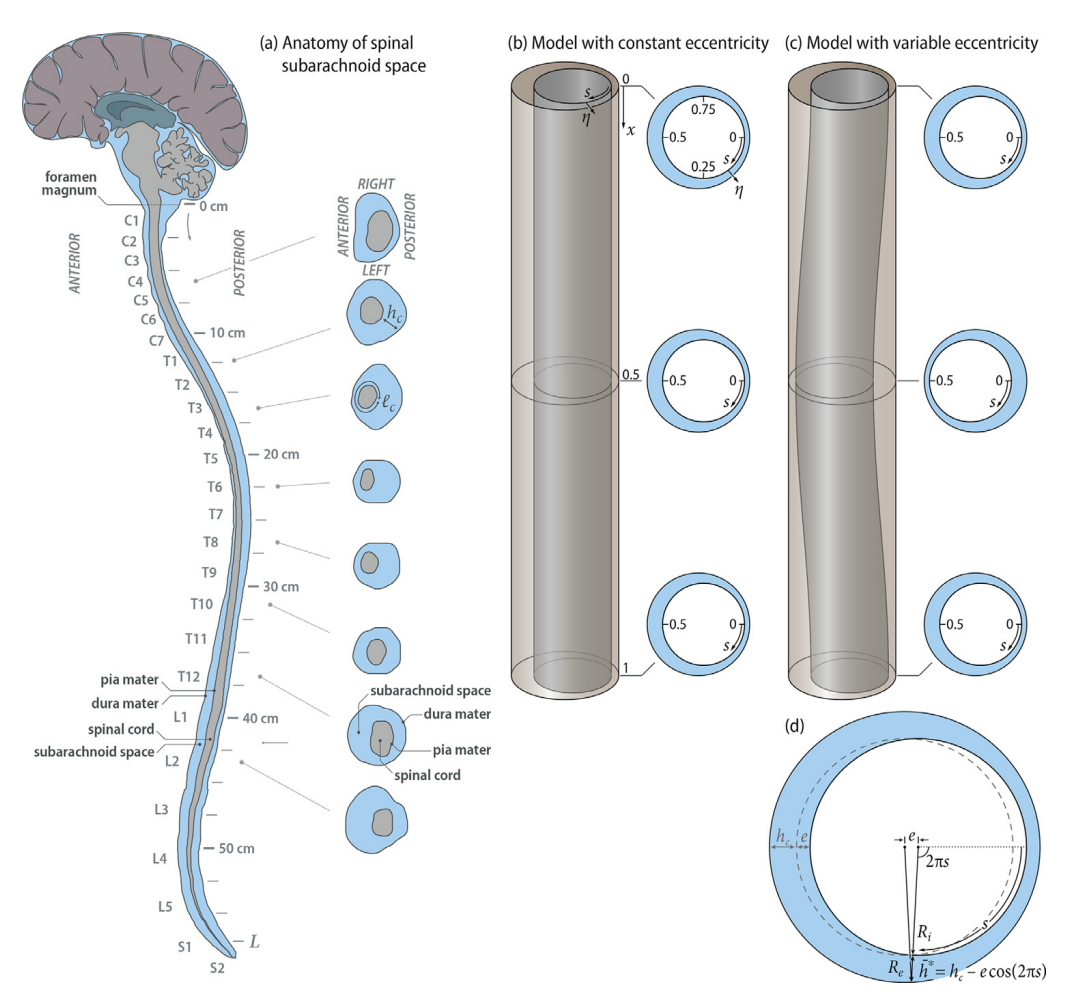


Fig. 1. Sketch of the geometrical configurations. (a) Anatomy of the spinal subarachnoid space (SSAS) extending from the foramen magnum to the sacrum. The figure shows several axial cuts at different locations. (b) Geometrical model with constant eccentricity indicating the curvilinear coordinates (x, s, η) . (c) Geometrical model with variable eccentricity. (d) Definition of the unperturbed canal width in the geometrical models.

fluctuations induced by the cardiac and respiratory cycles, has been reasoned to play a fundamental role in the physiological function of CSF as a vehicle for metabolic-waste clearance [1].

Attention will be focused here on the motion occurring in the spinal subarachnoid space (SSAS), a slender annular canal of length $L \simeq 60$ cm surrounding the spinal cord, represented schematically in Fig. 1(a). The canal is compliant, due to the presence of veins and fatty tissue in the surrounding dura membrane, which deforms in response to the local pressure fluctuations, allowing the motion of CSF in the closed canal. Understanding this fundamental fluid-structure interaction problem is needed, for instance, to properly comprehend substance and metabolite transport and distribution in the CNS [2], and to investigate the development of CNS diseases associated with pathological processes related to CSF disorders and neurodegenerative diseases [2-4]. A quantitative description of CSF flow is also fundamental to understand the implications of Chiari malformation [5-7] and its relation with the inception and growth of syringomyelia [8-10]. Furthermore, it is a fundamental element in developing quantitative predictions of drug dispersion in intrathecal drug delivery (ITDD) [11-13], a medical procedure used for treatment of some cancers [14], infections [15] and pain [16]. ITDD involves the delivery of a drug to the CNS by direct injection into the CSF, typically at an intraventricular, intracisternal, or lumbar site [13]. The lumbar route is most easily accessed and most commonly used. Although ITDD currently provides satisfactory results, the complex convective and diffusive mechanisms controlling the transport of the drug are not clearly understood, thereby limiting predictive capabilities concerning drug-delivery rates to targeted locations. Understanding of ITDD processes has been advanced in recent years through in-vivo experiments [17,18], in-vitro experiments [19,20], numerical simulations [21,22], or a combination of simulations and experimental measurements [23-25]. Despite these previous research efforts, there is still a pending need to develop reliable drug-dispersion predictive methodologies able to account for the specific anatomy and physiological conditions of the patient as well as the injection protocol and properties of the drug.

As revealed by in-vivo magnetic-resonance measurements [26,27], the pulsating velocity in the spinal canal displays peak values on the order of a few centimeters per second in the cervical region, decaying along the canal to vanish at its closed end in the sacral region. The time-averaged value of the velocity is not zero, but its magnitude is very small, on the order of a few centimeters per minute in the cervical region and smaller elsewhere in the canal. This slow motion plays a relevant

role in the transport of solutes carried by the CSF, such as metabolic-waste products and ITDD drugs. Resulting characteristic residence times, obtained by dividing the spinal-canal length by the characteristic time-averaged velocity, are on the order of 30 minutes, much larger than the characteristic times associated with the oscillatory flow (e.g. about one second for the motion driven by the cardiac cycle).

Computational efforts to describe the flow in the canal have addressed different aspects of the problem, as summarized in a recent paper by Khani et al. [25]. Fundamentally, the analysis involves a fluid-structure interaction problem, subject to boundary conditions that depend on the detailed anatomical features of the canal. Additional complications arise owing to the disparity of time scales present in the problem. For instance, quantification of solute dispersion, occurring over characteristic times on the order of 30 minutes, requires the description of hundreds of cycles, each one providing an infinitesimal contribution to the dispersion of the solute particles.

Recent theoretical efforts [28,29] have exploited the disparity of length and time scales present in the problem to develop a simplified description of the flow and of the associated solute transport rate. The complicated fluid-structure interaction problem was solved in the thin-film approximation [28], with the ratio ε of the stroke length to the canal length used as an asymptotically small parameter. The analysis, treating the SSAS as an unobstructed annular canal of slowly varying section and assuming a linear elastic model for the canal deformation, determines the motion of the CSF and the accompanying displacement of the dura membrane for a prescribed temporal variation of the intracranial pressure. In the first approximation, the Eulerian velocity is determined from a periodic linear lubrication problem that can be solved in closed form. In addition to this oscillatory flow, with zero time-averaged velocity at any location, it was found that the nonlinear terms associated with the convective acceleration and with the deformation of the canal introduce small corrections, leading to steady-streaming velocities that are a factor ε smaller than those of the oscillatory flow. This small steady velocity determines, together with the Stokes drift of the non-uniform pulsating flow, the slow time-averaged Lagrangian motion of the CSF particles, which was found in [29] to be responsible for the transport of the solute along the canal. A key outcome of the analysis is a time-averaged transport equation, given below in Eq. (10), which describes the solute evolution in the long-time scale. The use of the simplified equation effectively circumvents the need to integrate the complete problem over hundreds of oscillatory cycles, thereby reducing drastically the associated computational times.

The results of the theoretical analysis were previously used in [28] and [29] to investigate the motion and solute dispersion rate in a model of the canal with a simple geometry, shown in Fig. 1(b). The predictions were found to be in good qualitative agreement with accompanying in-vitro experimental measurements using flow visualizations enabled by neutrally buoyant fluorescent dye [28]. Validation through detailed quantitative comparisons with results of numerical integrations of the full transport equation was provided only for the case of a concentric annular canal [29], a simplified configuration of limited academic interest. Additional model assessments, including the important effect of azimuthal velocities (absent in the concentric canal), are needed to further validate the model, that being the purpose of the present paper. Here we will focus on the ability of the time-averaged model to circumvent the inherent complications stemming from the disparity of time scales present in the problem. This is a first necessary step in developing a comprehensive reduced-order model with sufficiently accurate predictive capabilities, to be ultimately used for optimization of drug delivery protocols. In that respect, it should be emphasized that, although the present model encompasses many of the essential physical mechanisms involved in the flow of CSF in the SSAS, there are additional important effects that should be considered in future work which are described in detail in Sec 5.

Fig. 1 (a) shows an illustration of the SSAS, including schematic views of the characteristic annular cross section at eight different positions. As can be seen, the position of the spinal cord relative to the dura mater changes along the canal, i.e. it is located close to the posterior side in the cervical region but close to the anterior side over most of the thoracic region, shifting back towards the posterior side as the lumbar region is approached. This variation of the eccentricity along the spinal canal within the anteroposterior plane has been shown to have an important effect on the motion of the cerebrospinal fluid and associated drug dispersion rate [27]. To investigate these effects, a simple geometrical model that exhibits variable eccentricity along the canal, shown in Fig. 1(c), will be considered in a second set of computations, aimed at validating the theoretical model under more relevant geometrical conditions.

We begin below by describing in Section 2 the formulation of the problem. Results corresponding to the model with constant eccentricity will be presented in Section 3, followed by the results for variable eccentricity in Section 4. The paper ends with concluding remarks in Sec 5.

2. Methods

2.1. Simplified representation of the spinal canal

The spinal canal is doubly slender, in that its length $L \simeq 500-600$ mm, characteristic perimeter $\ell_c \simeq 20-30$ mm, and characteristic width $h_c \simeq 3-4$ mm satisfy

$$h_c \ll \ell_c \ll L.$$
 (1)

As explained in [28] and [29], this slenderness condition enables a thin-film approximation in which terms that are of order $(\ell_c/L)^2$ and $(h_c/\ell_c)^2$ (and smaller) are neglected when writing the conservation equations, along with those associated with the small curvature along the spinal cord. The flow is described in terms of curvilinear coordinates (x, s, η) , where $x = x^*/L$

is the axial distance from the canal entrance scaled with L, s is the azimuthal distance normalized with the local perimeter, with $2\pi s$ being the corresponding azimuthal angle, and η is the transverse distance to the inner surface normalized with the local width, so that all coordinates vary from zero to unity. A sketch of the flow configuration with an indication of relevant coordinates is given in Fig. 1.

Following our previous theoretical developments [28,29], the present analysis will approximate the SSAS as an open annular canal, thereby neglecting the presence of micro-anatomical obstacles, such as trabeculae, ligaments, and nerve roots. Two geometrically simple configurations will be investigated, as sketched in Figs. 1 (b) and (c). The exterior surface surrounding the canal represents the dura membrane, while the interior surface represents the rigid pia mater surrounding the spinal cord. The deformation under pressure fluctuations of the veins and fatty tissue present in the dura membrane must be accounted for in analyzing the motion of the CSF, leading to a fluid-structure interaction problem that was previously solved on the basis of a linear elastic model [28,29]. The associated time-dependent displacements are small compared with the canal thickness, and can therefore be analyzed as small perturbations from an unperturbed state.

In this paper, the undeformed shape of the dura membrane will be taken to be a circular cylinder of radius R_e and length L. A circular cross section will also be assumed for the rigid inner surface surrounding the spinal canal, whose radius is $R_i = R_e - h_c$ with $h_c \ll R_e$. Correspondingly, in a plane perpendicular to the axis of the outer cylinder the annular canal is the space defined between two eccentric circles whose centers are separated by a small distance e, with $0 \le e \le h_c$, as indicated in Fig. 1(d). With small errors of order $h_c/R_e \ll 1$ the local undeformed width of the canal \bar{h}^* , measured normal to the inner surface, can be seen to be given by $\bar{h}^* = h_c - e \cos(2\pi s)$, with $0 \le s \le 1$. The configuration with two parallel cylinders of Fig. 1 (b), used in the illustrative computations of our previous analyses [28,29], corresponds to the case of constant eccentricity $e = \beta h_c$, with $\beta < 1$ representing a positive constant. The configuration in Fig. 1 (c), introduced here to investigate effects of variable eccentricity, considers the simple functional dependence $e/h_c = \beta \cos(2\pi x)$.

2.2. Slender-flow formulation for small stroke lengths

The oscillatory motion in the spinal canal is driven by the fluctuations of cranial pressure, associated with the cardiac and respiratory cycles. For simplicity, the cranial pressure oscillations are modeled with the simple harmonic function $(\Delta p)_c \cos(t)$, where $t = \omega t^*$ represents the time t^* scaled with the angular frequency $\omega = 2\pi/T$, with T being the period (i.e. $T \simeq 1$ s for the cardiac cycle and $T \simeq 5$ s for the respiratory cycle). Because of the presence of fatty tissue and veins, the dura membrane surrounding the subarachnoid space acts as an elastic wall that responds to the local pressure perturbations δp with small displacements δh , and can be described with a simple linear elastic model $\delta h = \gamma \delta p$, where $\gamma(x,s)$ represents a compliance factor. The model accommodates general axial and azimuthal variations of $\gamma(x,s)$, as needed to account for the non-uniform deformable nature of the dura membrane [30], enabling subject-specific studies in which the function $\gamma(x,s)$ can be determined from in-vivo MRI measurements of CSF flow, as done recently [27]. For the sake of simplicity, however, the following validation exercise is restricted to cases with constant γ .

The canal compliance is small in that the ratio

$$\varepsilon = \frac{\gamma (\Delta p)_c}{h_c} \sim \frac{L_s}{L} \ll 1 \tag{2}$$

of the characteristic dura-membrane displacement $\gamma(\Delta p)_c$ to the characteristic canal width h_c is small, resulting in an oscillatory motion with stroke lengths $L_s \sim 1$ cm, much smaller than the canal length $L \simeq 60$ cm, and corresponding characteristic streamwise velocities $u_c \sim \omega L_s \simeq \varepsilon \omega L$ on the order of a few cm/s. In particular, Coenen et al. [27] reported MRI-measured CSF peak velocities along the spinal canal between 7 cm/s (cervical zone) and 1.5 cm/s (lumbar zone) in a healthy human subject at a normal heart rate of 60 bpm, which yields stroke lengths between 2.2 cm and 0.5 cm, consistent with the order of magnitude $L_s \sim 1$ cm.

A simple order-of-magnitude analysis helps to clarify the main flow characteristics. The convective acceleration, whose order of magnitude is u_c^2/L , is a factor ε smaller than the local acceleration, of order ωu_c . On the other hand, the characteristic viscous time across the canal, h_c^2/ν , based on the typical value of the canal width $h_c \simeq 3-4$ mm [25,27,31,32], is on the order of 10–20 seconds, about 2–4 times larger than the period of the respiratory cycle and about 10–20 times larger than the period of the cardiac cycle. These estimates indicate that the viscous force per unit mass, although significantly smaller than the local acceleration, is still non negligible, and must be accounted for in the description. Viscous forces scale in the dimensionless formulation [28,29] with α^{-2} , where

$$\alpha = \left(\frac{h_c^2 \omega}{\nu}\right)^{1/2} \tag{3}$$

is the relevant Womersley number. Although α is of order 10 for the cardiac-induced motion, for consistency with the results presented earlier [28,29], most of the direct numerical simulations will be performed for flow conditions such that $\alpha = 3$.

The elastic behavior of the canal is characterized by the dimensionless wavenumber

$$k = \frac{\omega L}{[(h_c/\gamma)/\rho]^{1/2}} \sim 1,\tag{4}$$

involving the relevant elastic wave speed $[(h_c/\gamma)/\rho]^{1/2}$, which has been measured to be of the order of a few meters per second [33,34], yielding order-unity values of k.

In the previous theoretical developments, the problem was formulated by scaling the axial, azimuthal, and transverse velocities $\bar{v}^* = (u^*, w^*, v^*)$ with their characteristic values $\varepsilon \omega L$, $\varepsilon \omega \ell_c$, and $\varepsilon \omega h_c$ to give the order-unity variables (u, w, v). Similarly, the streamwise pressure difference from the entrance value is scaled with its characteristic value $\rho \varepsilon \omega^2 L^2$ to give the function p'(x,t), with the small pressure variations of order $\rho \varepsilon \omega^2 \ell_c^2$ that exist around the canal (i.e. at a fixed value of x) described by the accompanying dimensionless function $\hat{p}(x,s,t)$, needed in describing the azimuthal motion. The geometry of the canal is defined by the dimensionless functions $\ell(x)$ and $\ell(x)$ and $\ell(x)$ describing, respectively, the distribution of cord perimeter scaled with $\ell(x)$ and the instantaneous local value of canal width scaled with $\ell(x)$ for the configurations depicted in Figs. 1(b) and (c), to be used in the validation exercise, the dimensionless perimeter is just $\ell(x) = 1$, since the radius of the inner surface is constant, while the undeformed canal width is given, with small errors of order $\ell(x)$, by

$$\begin{cases} \bar{h} = 1 - \beta \cos(2\pi s) & \text{(constant eccentricity),} \\ \bar{h} = 1 - \beta \cos(2\pi s) \cos(2\pi x) & \text{(variable eccentricity),} \end{cases}$$
 (5)

to be used in the following computations. Because of the limited canal compliance, changes in the canal width from its unperturbed distribution $\bar{h}(x,s)$ are small, as described by the order unity deformation $h'(x,t)=(h-\bar{h})/\varepsilon$, related to the local pressure by the elastic equation

$$h'(x,t) = \cos t + k^2 p'(x,t).$$
 (6)

2.3. Description of the velocity field

The problem is solved for $\varepsilon \ll 1$ with $\alpha \sim 1$ and $k \sim 1$ by introducing regular asymptotic expansions in powers of ε for all variables (i.e. $u = u_0 + \varepsilon u_1 + \varepsilon^2 u_2 + \cdots$) [see 28]. At leading-order in the limit $\varepsilon \ll 1$, there exists a balance between the local acceleration, the pressure gradient, and the viscous forces, so that the zeroth-order functions are determined by a transient lubrication problem, coupled with the canal deformation through the linear elastic Eq. (6). Because of its linear character, the solution can be written in the form $u_0 = \text{Re}(\text{ie}^{\text{i}t}U)$, $w_0 = \text{Re}(\text{ie}^{\text{i}t}W)$, $v_0 = \text{Re}(\text{ie}^{\text{i}t}V)$, and $h_0' = \text{Re}(\text{e}^{\text{i}t}H)$, where the complex functions $U(x,s,\eta)$, $W(x,s,\eta)$, $V(x,s,\eta)$, and H(x) are evaluated as explained in the Appendix. In particular, the function H(x) describing the canal deformation, related to the streamwise pressure variation by $H = 1 + k^2 P$, as follows from Eq. (6), is determined by solving the boundary-value problem

$$\frac{1}{\ell} \frac{\mathrm{d}}{\mathrm{d}x} \left[\ell \left(\int_0^1 q \, \mathrm{d}s \right) \frac{\mathrm{d}H}{\mathrm{d}x} \right] + k^2 H = 0; \quad \begin{cases} H = 1 & \text{at } x = 0 \\ \frac{\mathrm{d}H}{\mathrm{d}x} = 0 & \text{at } x = 1 \end{cases}$$
 (7)

where

$$q(x,s) = \bar{h} - \frac{\sqrt{2}(1-i)}{\alpha} \tanh\left(\frac{\alpha \bar{h}}{2} \frac{1+i}{\sqrt{2}}\right). \tag{8}$$

For the configurations considered in Figs. 1(b) and (c) the solution simplifies, because $\ell=1$. Furthermore, for the case of constant eccentricity, the unperturbed canal width $\bar{h}=1-\beta\cos(2\pi s)$ is independent of x, and Eq. (7) can be solved exactly to give $H(x)=\cos[k(1-x)/(\int_0^1 q\mathrm{d}s)^{1/2}]/\cos[k/(\int_0^1 q\mathrm{d}s)^{1/2}]$. Its corresponding modulus, |H|, and argument, $\arg(H)$, are shown in Fig. 2 for k=0.5, $\alpha=3$ and $\beta=0.5$, along with those obtained for variable eccentricity by integration of Eq. (7). These two functions, determining the elastic wave travelling along the canal $h_0'(x,t)=|H|\cos[t+\arg(H)]|$, are used in the DNS computations to define the deformation of the dura membrane, as described below. For completeness, additional elastic-wave results are included as supplementary material.

The leading-order harmonic velocity has a zero average value, i.e. $(\langle u_0 \rangle, \langle w_0 \rangle, \langle v_0 \rangle) = (0, 0, 0)$, where $\langle \cdot \rangle = 1/(2\pi) \int_0^{2\pi} \cdot dt = 0$. As shown previously in [28], the first-order corrections (u_1, w_1, v_1) , arising from the nonlinear effects associated with convective acceleration and canal deformation, contain a steady component $(u_{SS}, v_{SS}, w_{SS}) = (\langle u_1 \rangle, \langle v_1 \rangle, \langle w_1 \rangle)$. Besides this steady-streaming velocity, the mean motion of the oscillating fluid particles contains a contribution arising from Stokes drift [29]. This is a purely kinematic effect associated with the spatial nonuniformity of the pulsatile flow. In the presence of a velocity gradient, a fluid particle subject to an oscillating velocity field experiences during each oscillatory cycle an instantaneous velocity that differs by a small amount from that existing at the initial point at corresponding times, so that it does not return to its original position at the end of the cycle. The small cyclical displacements accumulate in time to give the so-called Stokes drift, with associated steady velocities that are comparable to those of steady streaming. The sum of the steady-streaming velocity and the Stokes-drift velocity provides the steady time-averaged Lagrangian velocity,

$$(u_{L}, w_{L}, v_{L}) = (u_{SS} + u_{SD}, w_{SS} + w_{SD}, v_{SS} + v_{SD}), \tag{9}$$

that determines the slow motion of the fluid particles in the spinal canal. The steady-streaming velocity components (u_{SS}, v_{SS}, w_{SS}) and the Stokes-drift velocity components (u_{SD}, w_{SD}, v_{SD}) can be evaluated in terms of integrals involving U, W, V, and H, with associated expressions given in the Appendix.

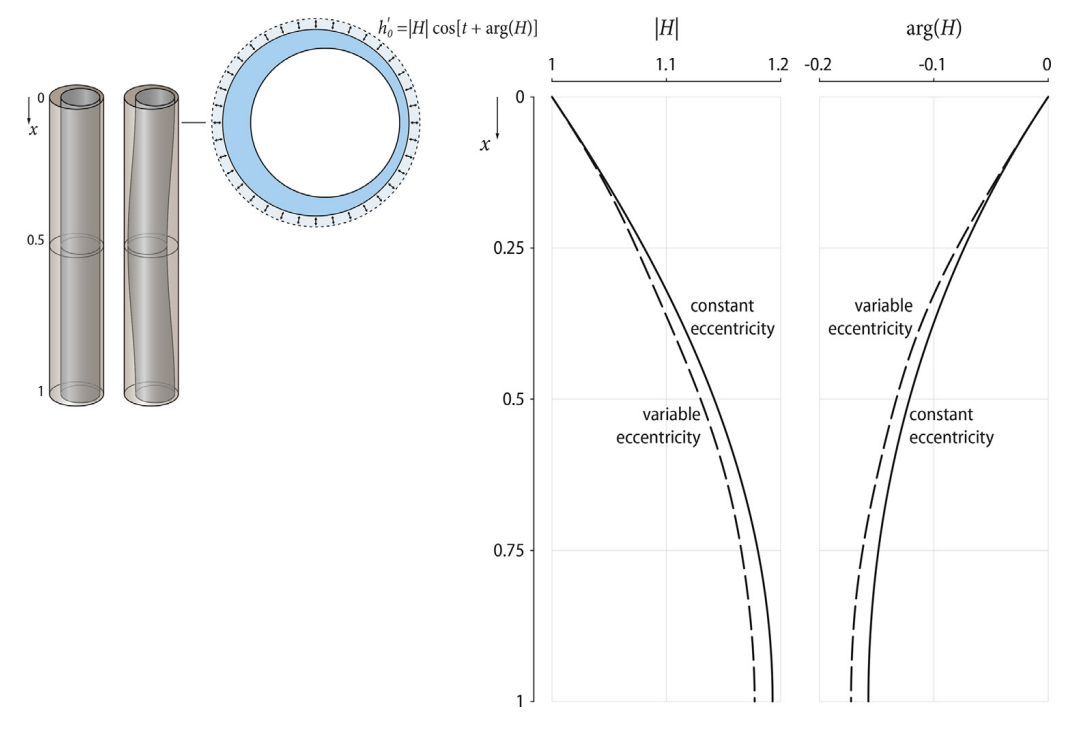


Fig. 2. Amplitude and phase of the wall displacement $h'_0(x,t) = |H| \cos[t + \arg(H)]$ resulting from the elastic wave that travels along the canal, for the model with constant eccentricity (solid line) and for that with variable eccentricity (dashed line). The corresponding instantaneous dimensionless canal width is given by $h(x, s, t) = \bar{h}(x, s) + \varepsilon h'_0(x, t)$.

2.4. Solute transport in the spinal canal

Our previous analysis [29] also considered the description of the transport of a solute with molecular diffusivity κ carried by the CSF. While the oscillatory motion of the CSF particles has a characteristic time ω^{-1} , the cumulative displacement along the canal associated with steady streaming and Stokes drift involves characteristic times of order $\varepsilon^{-2}\omega^{-1}$, that being the residence time obtained by dividing the characteristic spinal-canal length L by the characteristic magnitude of the streamwise Lagrangian velocity $\varepsilon u_c = \varepsilon^2 \omega L$. This disparity of time scales allows for a two-time-scale asymptotic description of solute transport to derive the following reduced equation, which will be used to describe the transport of drugs delivered intrathecally in the spinal canal in terms of the slow time variable $\tau = \varepsilon^2 t$,

$$\frac{\partial c_0}{\partial \tau} + u_L \left(\frac{\partial c_0}{\partial x} - \frac{\partial \bar{h}}{\partial x} \frac{\eta}{\bar{h}} \frac{\partial c_0}{\partial \eta} \right) + \frac{v_L}{\bar{h}} \frac{\partial c_0}{\partial \eta} + \frac{w_L}{\ell} \left(\frac{\partial c_0}{\partial s} - \frac{\partial \bar{h}}{\partial s} \frac{\eta}{\bar{h}} \frac{\partial c_0}{\partial \eta} \right) = \frac{1}{\alpha^2 \varepsilon^2 S \bar{h}^2} \frac{\partial^2 c_0}{\partial \eta^2}. \tag{10}$$

Here, $c_0(x, s, \eta, \tau)$ is the leading-order term in the expansion $c = c_0 + \varepsilon c_1 + \cdots$ for the solute concentration.

2.5. Direct numerical simulations

With the aim of providing detailed numerical results for validation of the theoretical model, three-dimensional, unsteady direct numerical simulations of the fluid motion and solute dispersion in the canal were carried out. To facilitate the computation, instead of using the intracranial pressure as input, the displacement of the dura membrane was prescribed, that also being the approach of the moving-boundary-motion method first used in the DNS computations of Tangen et al. (2015) [23] (see also Khani et al. 2018 [25]). For consistency, the nonuniform temporal distribution of the dura-membrane displacement was selected to be that found at leading order in the previous theoretical analysis of the fluid-structure interaction problem [28].

In the first stage of the computations, the Navier-Stokes equations for an incompressible Newtonian fluid,

$$\nabla \cdot \bar{v}^* = 0, \tag{11}$$

$$\frac{\partial \bar{v}^*}{\partial t^*} + \bar{v}^* \cdot \nabla \bar{v}^* = -\nabla p^* + \nu \nabla^2 \bar{v}^*,\tag{12}$$

were solved over many wall-displacement oscillation cycles until a periodic solution was attained. In the governing Eqs. (11) and (12) asterisks denote dimensional variables, and p^* represents the spatial pressure differences divided by the density. Numerically averaging the periodic Eulerian velocity $\bar{\nu}^*$ yields its steady-streaming component, which in turn

can be subtracted from \bar{v}^* to determine the zero-mean pulsating component of the velocity. Both are to be compared with the results of the asymptotic analysis presented before in Section 2.3. In the second stage of the computations, the transport problem

$$\frac{\partial c}{\partial t^*} + \bar{v}^* \cdot \nabla c = \frac{v}{S} \nabla^2 c,\tag{13}$$

was solved to study the slow-time dispersion of a solute, with the convective transport evaluated using the periodic velocity field determined from the first set of calculations. The initial spatial distribution of the solute, defined below in Eq. (15), is selected as representative of the release of a drug in the lumbar region. The simulations were extended over a large number of cycles, corresponding to values of the long-time scale τ of order unity, and their results are to be compared with those of the simplified transport problem (10). Note that in the computations, all terms in the conservation equations were retained, i.e. no simplifications on the basis of the slenderness of the canal or the smallness of the stroke length were introduced.

The numerical solution of Eqs. (11)–(13) was carried out with the finite-volume solver Ansys Fluent (Release 16.2), assuring second-order accuracy in time and in space. The PISO algorithm was used for the pressure-velocity coupling [35]. The no-slip conditions were imposed at the canal walls, and a condition of developed flow, $\nabla \bar{v}^* \cdot \bar{n} = 0$, was imposed at the inlet, where a buffer region of length 0.15L was added to avoid entrance effects. To model the deformation of the dura membrane, a dynamic mesh solver that employs a Laplacian mesh motion algorithm was used [25,36], with the instantaneous radius of the external boundary surface R_e varying from its unperturbed value R_e according to

$$R'_{e} = R_{e} + \varepsilon h_{c} h'_{0}(x^{*}/L, \omega t^{*}) = R_{e} + \varepsilon h_{c}|H|\cos[\omega t^{*} + \arg(H)]. \tag{14}$$

Here, the elastic-wave deformation $h'_0 = |H| \cos[\omega t^* + \arg(H)]$ was determined a priori by solving the linear fluid-structure interaction problem for a prescribed harmonic intracranial pressure fluctuation, as described before in Section 2.3. The specific functions |H| and $\arg(H)$ used in the simulations are those shown above in Fig. 2.

While the theoretical model is formulated in terms of dimensionless parameters, the DNS dimensional formulation requires specification of dimensional values for all parameters appearing in the equations and boundary conditions. In the integrations, the kinematic viscosity, appearing in Eqs. (12) and (13), was taken to be $\nu = 0.698 \times 10^{-6} \, \text{m}^2/\text{s}$, the value corresponding to water at 36.8° C. The dimensions of the domain for the two configurations shown in Figs. 1(b) and (c) are $L = 0.6 \, \text{m}$, $R_e = 5 \, \text{mm}$, and $R_i = 4 \, \text{mm}$, corresponding to a canal with characteristic width $h_c = R_e - R_i = 1 \, \text{mm}$ and constant inner perimeter $\ell_c = 2\pi R_i \simeq 25 \, \text{mm}$. In all computations, the dimensionless eccentricity is taken to be $\beta = 0.5$. The canal deformation, given in Eq. (14), is evaluated for an angular frequency $\omega = 2\pi \, s^{-1}$, as corresponds approximately to the cardiac cycle, with the function $H(x^*/L)$, shown in Fig. 2, computed with k = 0.5 and $\alpha = (h_c^2 \omega/\nu)^{1/2} = 3$, the latter value consistent with the parametric choice $h_c = 1 \, \text{mm}$, $\omega = 2\pi \, s^{-1}$, and $\nu = 0.698 \times 10^{-6} \, \text{m}^2/\text{s}$. In all computations, the reduced amplitude is taken to be $\varepsilon = 1/20$. It is worth noting that the canal thickness $h_c = 1 \, \text{mm}$ used in our computations, smaller than the typical values $h_c = 3 - 4 \, \text{mm}$ reported in the literature [25,27,31,32], was chosen to give a value of $\alpha = 3$, consistent with results presented earlier [28,29]. Consideration of more realistic values of $h_c \sim 3 \, \text{mm}$ would lead to larger values of the model predictions from the DNS results are expected to increase for increasing values of h_c/R_i , the predictive capability of the model remains valid, provided that the condition $h_c \ll l_c$ is satisfied.

The computational domain was discretized using a structured uniform mesh. A grid sensitivity analysis was conducted to ensure the grid-size independence of the results. To that end, integrations were sequentially performed with an increasing number of grid points, starting from a coarse grid with 7.5×10^4 computational cells. In comparing results corresponding to different grids, the periodic velocity field was characterized by the amplitude of the axial velocity oscillation $(u_{\max}^* - u_{\min}^*)$ at two locations of the anteroposterior plane, namely, $x^* = L/2$ (x = 1/2), $y^* = \bar{h}/2$ $(\eta = 1/2)$ and s = 0 and s = 0.5. This velocity amplitude was seen to decrease as the number of grid point increases, with relative changes becoming progressively smaller. The transport of the solute was also assessed by comparing axial distributions of averaged concentration at different x-sections. Differences in concentration profiles were quantified with the discretized version of the L_2 -norm $||f-g||_2 = [\int_0^1 (f-g)^2 \mathrm{d}\eta]^{1/2}$. The refinement was continued until the relative differences resulting from doubling the number of grid points in consecutive computations were less than 0.3% for the velocity and less than 1% for the concentration. The final configuration selected, to be used in the computations presented below, contains a total of 1.95×10^6 grid points.

In the following, results from the simulations will be compared with those of the previous theoretical analyses. The steady-streaming velocity components u_{SS} and w_{SS} will be evaluated from the DNS results by taking the time averages $\langle u^* \rangle = \omega/(2\pi) \int_0^{2\pi/\omega} u^* \, dt^*$ and $\langle w^* \rangle = \omega/(2\pi) \int_0^{2\pi/\omega} w^* \, dt^*$, and scaling the resulting axial and azimuthal components with their characteristic values $\varepsilon^2 \omega L$ and $\varepsilon^2 \omega \ell_c$, respectively. These values are compared below with the theoretical predictions $u_{SS} = \langle u_1 \rangle$ and $w_{SS} = \langle w_1 \rangle$ stemming from the asymptotic analysis. Similarly, the harmonic leading-order velocity components predicted by the linear lubrication problem, $(u_0, w_0) = \text{Re}\big[i e^{it} (U, W)\big]$, will be compared with the corresponding DNS predictions for the purely oscillatory flow, obtained by subtracting its mean value according to $u^* - \langle u^* \rangle$ and $w^* - \langle w^* \rangle$, and scaling the resulting axial and azimuthal velocity components with their characteristic values $\varepsilon \omega L$ and $\varepsilon \omega \ell_c$. Additional results will be presented for the time-dependent dispersion of a solute, with results of integrations of the full transport Eq. (13) compared with those of the simplified Eq. (10) for different values of the Schmidt number S.

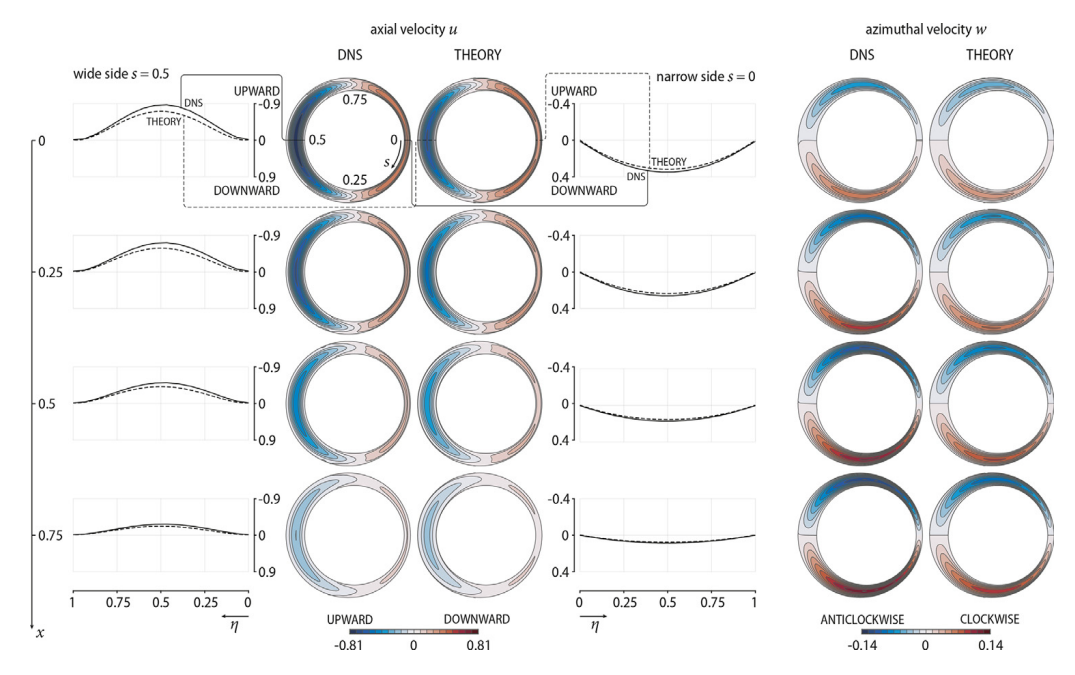


Fig. 3. Comparison of the oscillatory velocity determined in the numerical simulations with that predicted by the simplified model. The theoretical predictions are evaluated from the analytical expressions $u_0 = \text{Re}\big[i\mathrm{e}^{it}U(x,\eta,s)\big]$ and $w_0 = \text{Re}\big[i\mathrm{e}^{it}W(x,\eta,s)\big]$, with the normalized transverse coordinate η taken to be perpendicular to the inner surface. To enable quantitative comparisons to be made, the DNS results are represented in their dimensionless form $(u^* - \langle u^* \rangle)/(\varepsilon \omega L)$ and $(w^* - \langle w^* \rangle)/(\varepsilon \omega \ell_c)$ with $\ell_c = 2\pi R_i$.

3. Results with constant eccentricity

We begin in this section by presenting results for the constant-eccentricity model shown in Fig. 1(b), also addressed in our previous publications, with the case of variable eccentricity investigated in the following section.

3.1. Pulsating velocity fields

The axial and azimuthal components of the oscillatory velocity obtained in the DNS computations, expressed in the dimensionless form $(u^* - \langle u^* \rangle)/(\varepsilon \omega L)$ and $(w^* - \langle w^* \rangle)/(\varepsilon \omega \ell_c)$, are compared in Fig. 3 with the theoretical predictions $(u_0, w_0) = \text{Re} \big[\text{ie}^{\text{it}}(U, W) \big]$. Velocity distributions are given for $t = \omega t^* = \pi$ at four different sections x = (0, 0.25, 0.5, 0.75). In plotting the theoretical predictions, the coordinate η is measured perpendicular to the inner surface. Note that upward (cranial) / downward (caudal) flow corresponds to negative / positive values of the axial velocity.

As expected, the flow is symmetric with respect to the symmetry plane of the canal, defined by s = 0 and s = 0.5. The magnitude of the axial velocities is seen to decrease with the axial coordinate, to eventually vanish at the closed end of the canal x = 1 [28]. By way of contrast, the magnitude of the azimuthal velocity, shown on the right-hand side of the figure, tends to increase along the spinal canal, as needed to accommodate the flow recirculation.

At the instant of time $t = \omega t^* = \pi$ selected in the figure, the flow moves downwards in the narrow part of the canal and upwards in the wide part. Since viscous effects are more prominent in the narrow regions (i.e. around s = 0), the largest peak velocities are found at s = 0.5. The time-dependent evolution of the velocity, shown in a movie included as supplementary material, displays the expected wave-like behavior, associated with the canal deformation described by Eq. (14).

To enable a more precise quantitative comparison, profiles of axial velocity are plotted across the canal at s=0.5 (left) and s=0 (right). The velocity profiles obtained analytically are symmetric in both locations, since the model does not take into account curvature effects. However, the numerical results, obtained with large but finite curvature $R_i/h_c=4$, display slight asymmetries, with peak velocities lying closer to the inner surface $\eta=0$. The relative difference in centerline velocity, measured by the value of $|u_0-(u^*-\langle u^*\rangle)|/|u_0|$ at $\eta=0.5$, varies over the course of the oscillation cycle. This relative difference is of the order of 9% when the flow rate is maximum at $t=\pi/2$ (upward flow) and at $t=3\pi/2$ (downward flow) and of the order of 15% when the flow rate reverses direction at t=0 and $t=\pi$, the flow in the latter instant of time being represented in Fig. 3. As explained later in the discussion of Fig. 5, both the small asymmetries and the departures in the velocity values are associated with curvature effects resulting from the finite value of the slenderness ratio h_c/R_i .

3.2. Steady streaming

The predictions $u_{SS} = \langle u_1 \rangle$ and $w_{SS} = \langle w_1 \rangle$ for the axial and azimuthal components of the steady-streaming velocity, evaluated from the expressions given in the Appendix, are compared in Fig. 4 with the time-averaged values of the DNS

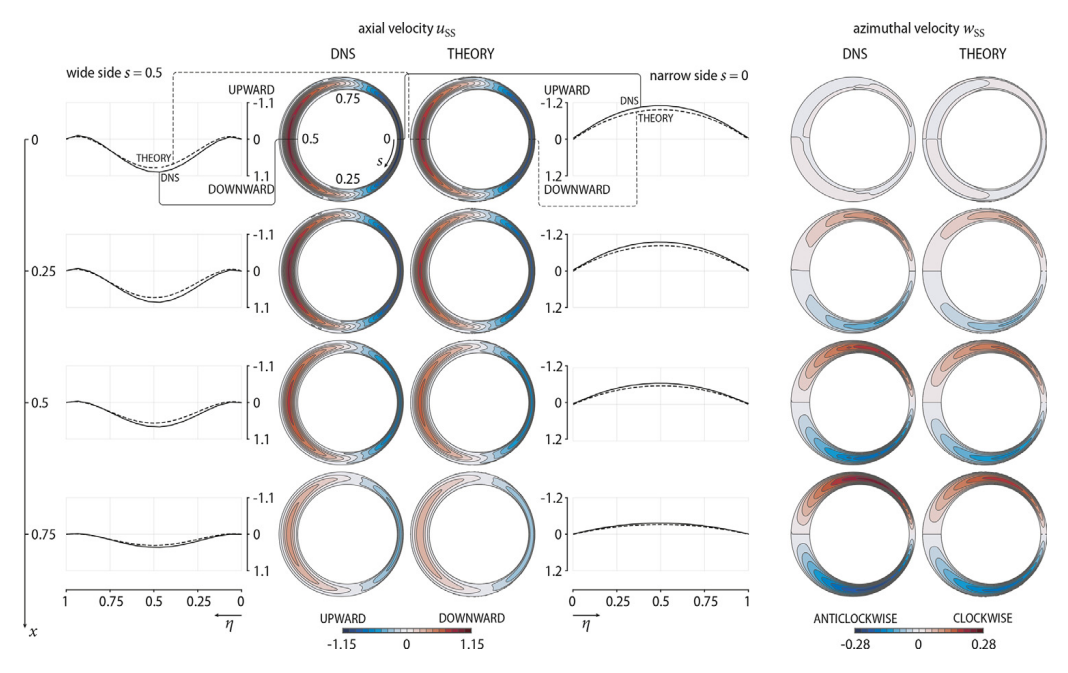


Fig. 4. Comparison of the steady-streaming velocity components u_{SS} and w_{SS} determined numerically with those predicted by the simplified model. The theoretical predictions are evaluated using the expressions $u_{SS} = \langle u_1 \rangle (x, \eta, s)$ and $w_{SS} = \langle w_1 \rangle (x, \eta, s)$ given in Appendix A.2, with the normalized transverse coordinate η taken to be perpendicular to the inner surface. To enable quantitative comparisons to be made, the DNS results are represented in their dimensionless form $u_{SS} = \langle u^* \rangle / (\varepsilon^2 \omega \ell_c)$ and $w_{SS} = \langle w^* \rangle / (\varepsilon^2 \omega \ell_c)$ with $\ell_c = 2\pi R_i$.

velocities, expressed in the dimensionless form $u_{\rm SS} = \langle u^* \rangle / (\varepsilon^2 \omega L)$ and $w_{\rm SS} = \langle w^* \rangle / (\varepsilon^2 \omega \ell_c)$, as needed for consistency. Good agreement is again found between the theoretical predictions and the numerical results, with relative differences in peak values remaining below 15%. As can be inferred from the transverse profiles of $u_{\rm SS}$ at s=0 and s=0.5, the magnitude of the steady-streaming velocities computed in the direct numerical simulations is slightly larger than that predicted by the analytical model. As explained below, the observed departures, on the order of 10% to 15%, can be attributed to the different approximations incorporated in developing the analytical results, as well as the finite slenderness of the geometry. Although the results presented here have been obtained for $\alpha=3$, preliminary direct numerical simulations at $\alpha=10$ also corroborate the good agreement between the theoretical and the numerical results at more realistic Womersley numbers, commonly observed in human beings.

The resulting axial velocities are found to be mainly positive (downwards) where the canal width is larger (i.e. values of s around s = 0.5) and mostly negative (upwards) where the canal width is smaller (i.e. values of s around s = 0), in agreement with previous results. The flow is symmetric with respect to the plane s = 0 and s = 0.5, where $w_{SS} = 0$, with the fluid moving azimuthally in the direction of decreasing canal width. It is of interest that the magnitude of u_{SS} decreases away from the entrance (i.e. for increasing values of s) while that of s0 increases, as needed to accommodate flow recirculation.

The small discrepancies observed between the numerical simulations and the theoretical predictions can be attributed to the simplifications introduced in developing the theoretical model. To investigate the inaccuracies associated with the assumption of slender flow, stated in Eq. (2), computations were performed in more slender canals with smaller widths $h_c = R_e - R_i$, such that $h_c/R_i = 1/8$ and $h_c/R_i = 1/40$. Resulting profiles of axial velocity at x = 0.5 and s = 0.5 are plotted in Fig. 5 along with those of the previous calculations, corresponding to $h_c/R_i = 1/4$. The pulsating and time-averaged components $(u^* - \langle u^* \rangle)/(\varepsilon \omega L)$ and $\langle u^* \rangle/(\varepsilon^2 \omega L)$ are compared with the functions u_0 and $\langle u_1 \rangle$. As can be seen, as effects of curvature become less important for decreasing values of h_c/R_i , the associated DNS profiles become more symmetric and tend to approach the theoretical prediction. For instance, when the canal thickness is reduced to $h_c/R_i = 1/40$, the peak values of the pulsating and time-averaged velocity components predicted by the model differ by only 1.5% and 3.5% from the corresponding DNS values.

The long-term Eulerian bulk flow induced by the steady streaming can be characterized by representing on an s-x plane the streamlines associated with the width-averaged values of the axial and azimuthal velocity components $\int_0^1 u_{\rm SS} {\rm d}\eta$ and $\int_0^1 w_{\rm SS} {\rm d}\eta$. Results corresponding to the computation of Fig. 4 are shown on the left-hand side of Fig. 6, with small arrows added to indicate the direction of the flow. The separation between streamlines characterizes the velocity magnitude, with smaller spacing corresponding to larger speeds. The resulting streamlines are very similar to those corresponding to the theoretical predictions, represented in the accompanying right-hand-side plot (Fig. 6b). The streamlines help visualize the flow features previously discussed. The fluid is seen to enter along the wide part of the canal and leave along the narrow part, recirculation occurring at a faster rate towards the closed end, in agreement with the velocity contours shown in Fig. 4.

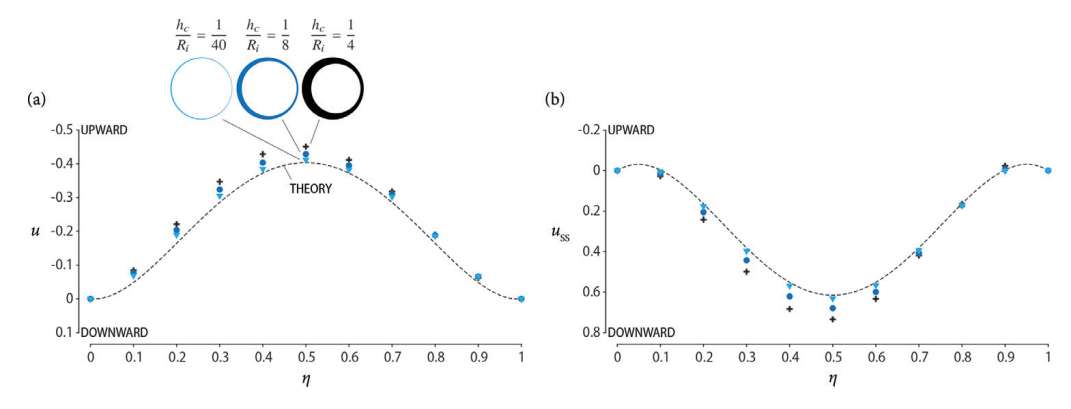


Fig. 5. Profiles of axial velocity at x=0.5 and s=0.5 for three different values of h_c/R_i , including the instantaneous pulsating component $(u^* - \langle u^* \rangle)/(\varepsilon \omega L)$ evaluated at $t=\omega t^*=\pi$ (a), and the time-averaged component $u_{\rm SS}=\langle u^* \rangle/(\varepsilon^2 \omega L)$ (b). The dashed lines represent the corresponding theoretical predictions u_0 and $\langle u_1 \rangle$.

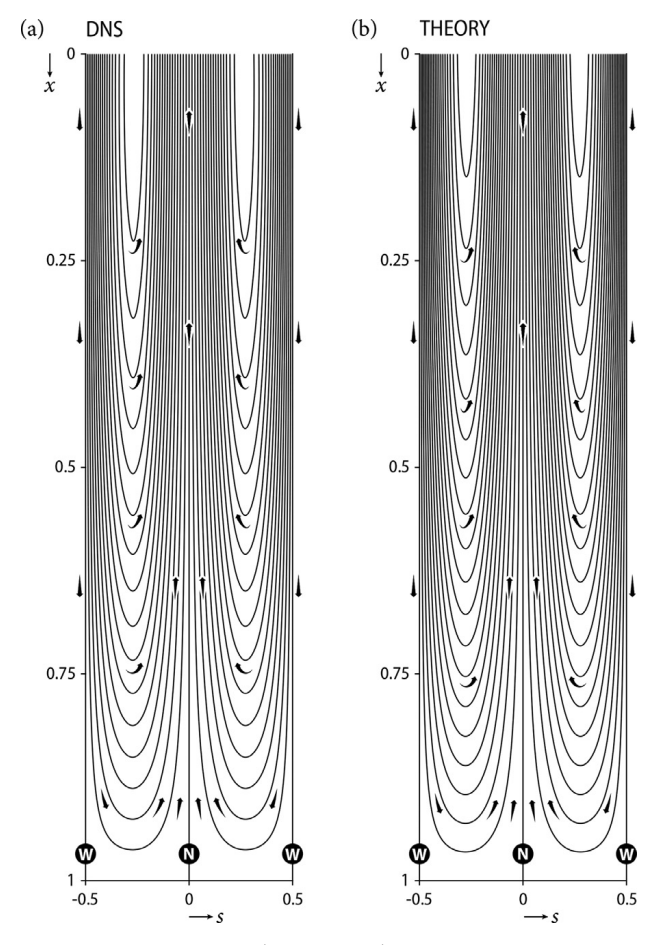


Fig. 6. Streamlines corresponding to the width-averaged velocities $\int_0^1 u_{SS} d\eta$ and $\int_0^1 w_{SS} d\eta$ for the flow conditions of Fig. 4. The letters N and W near the bottom indicate the azimuthal location of the narrowest and widest sections.

3.3. Solute dispersion

To test the accuracy of the theoretical model in describing transport in the spinal canal, we consider the temporal evolution of a bolus of solute released at the initial instant of time. The initial concentration is given by the truncated Gaussian distribution

$$c(x^*/L) = \min\left\{1, \frac{3}{2} \exp\left[-16^2 \left(\frac{x^*}{L} - \frac{3}{4}\right)^2\right]\right\},\tag{15}$$

selected as representative of injection of a solute bolus in the upper lumbar region. The initial profile (15), representing a band of saturated solute flanked by thin regions with concentration decay, is selected for convenience and comparison

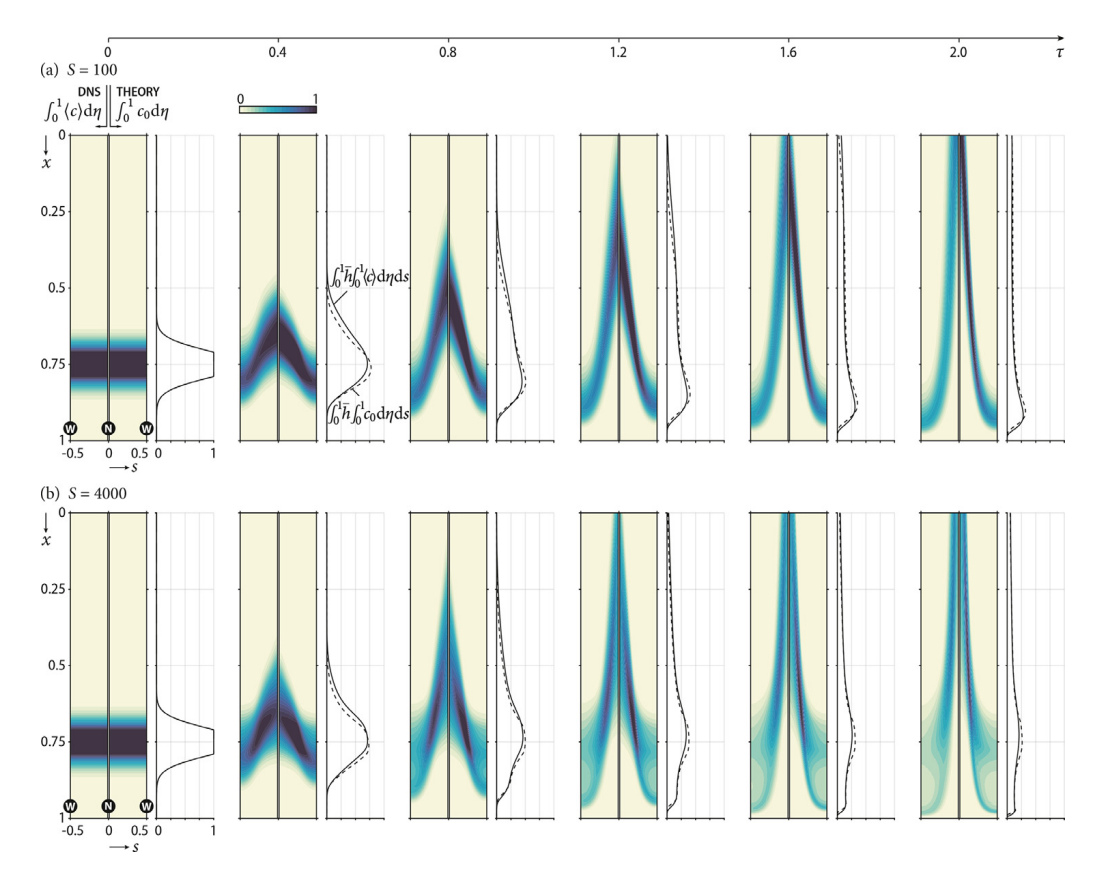


Fig. 7. Width-averaged distributions of concentration at different instants of time following the release of a bolus of solute with Schmidt number S = 100 (a) and S = 4000 (b) in the constant-eccentricity canal of Fig. 1(b). Flow conditions correspond to those in Figs. 3 and 4. DNS results are represented by the contours on the left-hand side of the panels and by the solid curves representing the axial distribution of solute on the side plots. Theoretical predictions corresponding to integrations of Eq. (10) are represented by the contours on the right-hand side of the panels and by the dashed curves on the side plots. The letters N and W near the bottom of the leftmost panels indicate the azimuthal location of the narrowest and widest sections.

purposes between the model and the DNS results. Clearly, the specific shape of the initial concentration depends on the details of the injection protocol. Its influence on the resulting transport history should be further investigated in future work. In that regard, the reader is referred to the work of Tangen et al. [20] for a comprehensive computational and in-vitro experimental study of the effects of injection volume, including additional effects of drug-tissue chemical interaction.

Predictions obtained by integrating the time-averaged Eq. (10) in the long time scale $\tau = \varepsilon^2 t = \varepsilon^2 \omega t^*$ for $0 \le \tau \le 2$ are compared in Fig. 7 with results of integrations of Eq. (13) for $0 \le \omega t^* \le 800$. The figure shows distributions of width-averaged concentration for different times, together with the corresponding axial distributions of the averaged concentration at each section x, computed according to $\int_0^1 (\bar{h} \int_0^1 \langle c \rangle d\eta) ds$ and $\int_0^1 (\bar{h} \int_0^1 c_o d\eta) ds$ for the DNS and the model, respectively. Here, $\langle c \rangle = \omega/(2\pi) \int_{t^*}^{t^*+2\pi/\omega} c(\bar{x}^*, t^*) dt^*$ indicates the time-averaged value of the concentration over a cardiac cycle. The results correspond to the flow conditions of Figs. 3 and 4 for two different values of the Schmidt number, namely S = 100 and S = 4000.

The agreement between the numerical results and those given by the model is very satisfactory. Relative differences in axial distributions of averaged concentration, measured with the L_2 -norm $||\int_0^1 (\bar{h} \int_0^1 \langle c \rangle \, d\eta) \, ds - \int_0^1 (\bar{h} \int_0^1 c_0 \, d\eta) \, ds||_2 = \{\int_0^1 [\int_0^1 (\bar{h} \int_0^1 \langle c \rangle \, d\eta) \, ds - \int_0^1 (\bar{h} \int_0^1 c_0 \, d\eta) \, ds]^2 dx\}^{1/2}$, were seen to remain below 0.05 (S=100) and 0.04 (S=4000) throughout the duration of the computations. These small differences can be mainly attributed to the aforementioned discrepancies in the pulsatile and steady-streaming velocity profiles.

The comparisons in Fig. 7 clearly demonstrate the predictive capability of the reduced transport Eq. (10), involving the combined effects of convection, driven by the time-averaged Lagrangian velocity, and molecular diffusion across the width of the canal. As expected from the streamline pattern shown in Fig. 6, the solute is convected along the narrow part of the canal (s = 0), reaching the canal entrance at $\tau = \varepsilon^2 t \approx 1.2$. This fast upward motion is accompanied by a slower downward motion occurring along the wide part of the canal (s = 0.5). This result is consistent with the findings of Tangen et al. [17], who have recently shown a fast caudocranial motion in-vivo experiments in cynomolgus monkeys.

The theoretical model is seen to appropriately capture the effects of solute diffusivity, described in the time-averaged Eq. (10) by the transverse-diffusion term on the right-hand side, leading to solute spatial distributions that are different for S = 100 and S = 4000, with theoretical predictions in good quantitative and qualitative agreement with the DNS results.

In explaining the differences in solute dispersion between these two different Schmidt numbers, one should bear in mind that the extent of transverse diffusion depends on the value of $\alpha^2 \varepsilon^2 S$, the ratio of the transverse diffusion time h_c^2/κ to the characteristic residence time $\varepsilon^{-2}\omega^{-1}$ associated with the mean Lagrangian motion. For the values $\alpha=3$ and $\varepsilon=0.05$ considered here, this time ratio becomes $\alpha^2 \varepsilon^2 S = 90$ for S = 4000 and $\alpha^2 \varepsilon^2 S = 2.25$ for S = 100, indicating that transverse diffusion is significant for S = 100 but largely absent for S = 4000. In the former case, diffusion tends to uniformize the solute concentration in the transverse direction η , so that convective transport occurs with the width-averaged Lagrangian velocity, resulting in the plots of width-averaged concentration maps shown in Fig. 7(a). In contrast, for S = 4000 each individual fluid particle moves with a nearly constant concentration. Particles near the pia and dura membranes, where the Lagrangian velocity vanishes, tend to stay stagnant, while those located near $\eta = 0.5$, where the velocity peaks, move fast, contributing to the dispersion of the solute. The width-averaged concentration maps shown in Fig. 7(b) are a consequence of this differential convective transport, which has a more pronounced effect on the wide side of the canal (i.e. s = 0.5), where the transverse diffusion time is largest. Perhaps counterintuitively, the resulting solute dispersion rate for S = 4000 is larger than that for the less diffusive case S = 100, as can be seen by comparing the maps of solute concentration in Fig. 7(a) and (b). The comparison reveals, in particular, that the rate of solute-front propagation along the canal from the injection location, both towards the entrance x = 0 and towards the closed end x = 1, is faster for S = 4000 than for S = 100. This can be explained by recalling that for S = 100 the solute front moves along the canal at a rate given approximately by the width-averaged Lagrangian velocity, that being a result of the uniformizing effect of transverse diffusion. By way of contrast, in the less diffusive case S = 4000 the evolution of the solute front is largely determined by the motion of the fluid particles located near the canal center $\eta = 0.5$, which move at a velocity that exceeds the mean value, thereby explaining the faster front-propagation rate.

The interplay between convection and transverse diffusion also affects the axial distribution of solute concentration $[\int_0^1 (\bar{h} \int_0^1 c_0 d\eta) ds]$, depicted on the side plots next to the two-dimensional maps of Fig. 7. An interesting finding is that smaller diffusivities appear to yield greater equilibration of concentration, in that the peak values of $[\int_0^1 (\bar{h} \int_0^1 c_0 d\eta) ds]$ are somewhat lower for S = 4000, that being a result of the rapid dispersion associated with the motion of the individual fluid particles, moving with nearly constant concentration. Also, while for S = 100 the peak values are seen to migrate towards x = 1, driven by the convective flow, for S = 4000 they do not move far from x = 0.75, because a large amount of solute remains at the injection location on the wide side of the canal (i.e. around s = 0.5), trapped in slow moving near-wall layers. It is worth emphasizing that all of these nontrivial effects of solute diffusivity are a consequence of the interplay of transverse diffusion with the time-averaged Lagrangian motion, while solute diffusion in the axial and azimuthal direction plays a negligible role, as demonstrated by the good agreement between the DNS results and the theoretical predictions based on the model transport Eq. (10).

4. Results with variable eccentricity

To investigate effects of nonuniform eccentricity of the canal section, additional integrations were performed for the model geometry shown in Fig. 1(c). Streamlines corresponding to the width-averaged values $\int_0^1 u_{\rm SS} {\rm d} \eta$ and $\int_0^1 w_{\rm SS} {\rm d} \eta$ of the axial and azimuthal velocity components are shown in Fig. 8. As can be seen, the theoretical predictions are in good agreement with the DNS results. The resulting flow pattern, including three recirculating regions, is markedly different from that shown previously in Fig. 6 for constant eccentricity. The flow direction is reversed between contiguous recirculating cells, so that in the top and bottom regions the flow is downwards at s=0.5 and upwards at s=0, while in the intermediate region the flow is upwards at s=0.5 and downwards at s=0.5 around which the flow exhibits a local counterflow configuration. The streamline spacing is used to indicate the magnitude of the velocity, which shows very different values in the different regions, smaller at larger distances from the entrance. The results indicate that the time-averaged motion is virtually absent in the bottom recirculating region, where the velocities are three orders of magnitude smaller than those found in the top recirculating region, in agreement with previous findings [27].

The existence of unconnected closed recirculating regions has a dramatic effect on the solute dispersion along the canal, as verified in accompanying integrations of the transport Eq. (13) with the initial condition stated in Eq. (15). These DNS results are shown in Fig. 9, along with predictions obtained with the simplified transport Eq. (10). As can be seen, the model properly describes the transport of the solute along the canal. The resulting maximum values of the L_2 -norm differences in axial distributions of the averaged concentration (0.08 for S = 100 and 0.06 for S = 4000) are somewhat larger than those previously obtained for constant-eccentricity (0.05 for S = 100 and 0.04 for S = 4000), the increase being attributable to the added complexity of the flow.

According to the streamline pattern shown in Fig. 8, the initial distribution of solute, given in Eq. (15), is centered at $x^*/L = 0.75$, so that the bolus occupies initially a section of the canal lying between the bottom and central vortices. As a consequence, the upper and lower sides of the bolus are subject to a recirculating flow with opposite sign, eventually resulting in counterflowing convective transport along the line s = 0.5, with the solute carried by the central vortex moving upwards and the solute carried by the bottom vortex moving downwards. The subsequent temporal evolution of the solute demonstrates the dominant role of Lagrangian convection, with the solute largely following the streamlines of Fig. 8. In the absence of molecular diffusion, solute particles would remain trapped in the central and bottom recirculating regions.

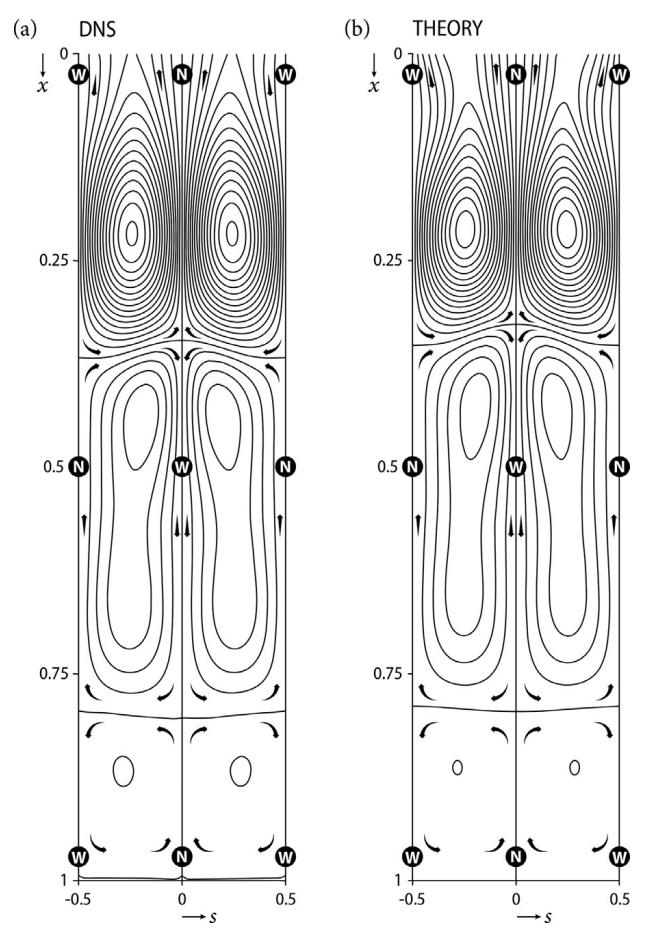


Fig. 8. Streamlines corresponding to the width-averaged velocities $\int_0^1 \langle u_{SS} \rangle d\eta$ and $\int_0^1 \langle w_{SS} \rangle d\eta$ for the variable-eccentricity model geometry of Fig. 1(c). The letters N and W indicate the azimuthal location of the narrowest and widest sections respectively.

The DNS results reveal that diffusive transport provides limited inter-vortex connectivity, enabling a small portion of solute to reach the entrance of the canal at the end of the numerical integration, as shown in Fig. 9. Since axial and azimuthal diffusion fluxes are neglected in the model, vortex connectivity relies on the action of transverse diffusion across overlapping streamlines near the vortex separating interface, with the consequence that the amount of solute reaching the entrance of the canal is underpredicted. Additional mixing induced by the presence of microanatomical features, not accounted for in the model, can be expected to provide additional inter-vortex connectivity, an aspect of the problem to be investigated in future work.

The distribution of solute along the canal also differs with the Schmidt number. For S = 4000, the solute covers a wide part of s = 0.5 and a surrounding area along the central and lowest recirculating regions, whereas for S = 100 it concentrates closer to s = 0.5 (and subsequently s = 0), caused by the effect of the transverse molecular diffusion for that S. In fact, since the molecular diffusion is negligible for S = 4000, the azimuthal convection becomes more relevant, dispersing the solute along S. Some studies have also reported the absence of solute rostral flow [18,20,37], which limits the presence of solute at the posterior region, similarly to what is found here for S = 4000. This result has also been argued to partly depend on the physicochemical characteristics of the solute.

An interesting aspect related to balance between transverse diffusion and convection around the separatrix between the bottom and central vortices is the peak of concentration observed in the results given by the model, displayed in Fig. 9(a). The initial time evolution of the solute boluses are similar for S = 100 and S = 4000, dispersing upstream and downstream from the injection point around s = 0.5 and decreasing their thickness around x = 0.75. However, at longer times the solute is convected axially and azimuthally for Schmidt number S = 4000, while it remains in two thin layers at x = 0.75 and close to s = 0.5 in the central vortex for S = 100. Since the axial, radial and azimuthal velocities are nearly zero around x = 0.75, transverse diffusion dominates in this region, equilibrating the concentration in the radial direction, which translates in the thin peak of solute concentration shown in Fig. 9(a). However, at larger values of S, transverse diffusion becomes negligible, and the convective terms in Eq. (10) dominate the process, dispersing the solute axially and azimuthally before it is tranversally diffused.

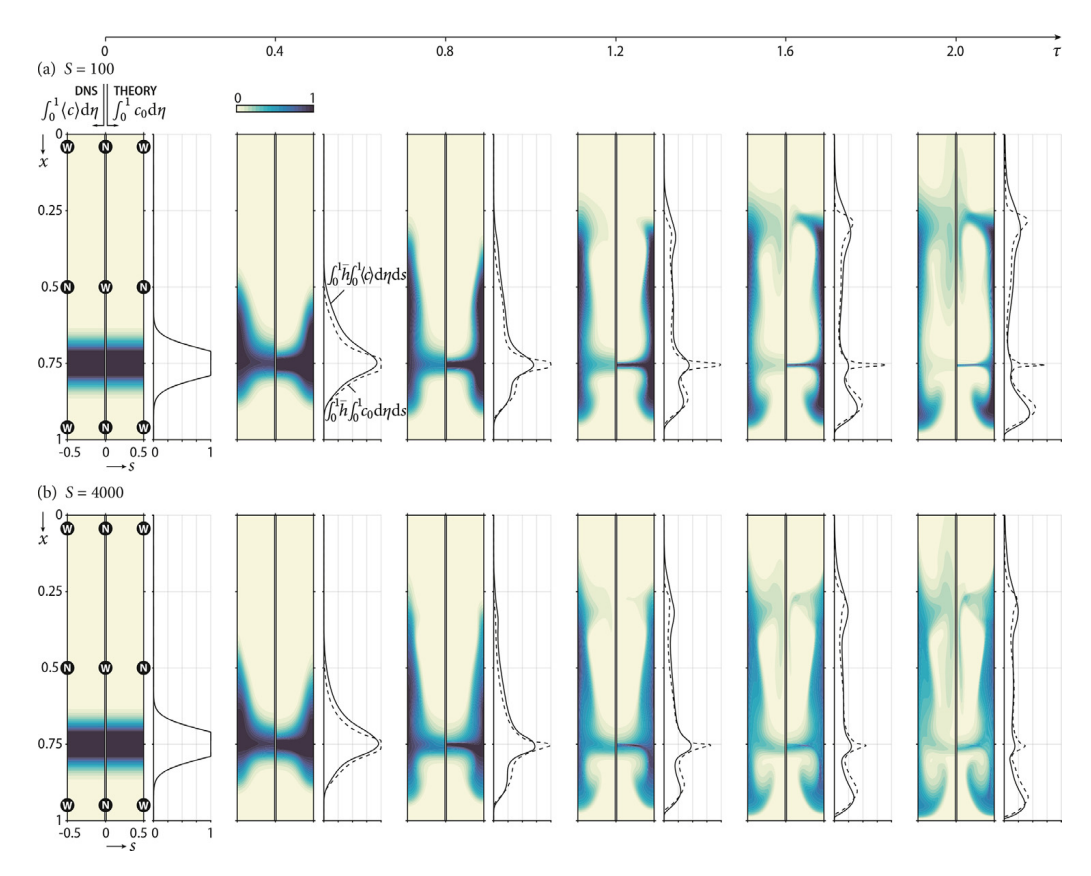


Fig. 9. Width-averaged distributions of concentration at different instants of time following the release of a bolus of solute with Schmidt number S = 100 (a) and S = 4000 (b) in the variable-eccentricity canal of Fig. 1(c). The solute is carried by the flow depicted in Fig. 8. DNS results are represented by the contours on the left-hand side of the panels and by the solid curves representing the axial distribution of solute on the side plots. Theoretical predictions corresponding to integrations of Eq. (10) are represented by the contours on the right-hand side of the panels and by the dashed curves on the side plots. The letters N and W at the leftmost panels indicate the azimuthal location of the narrowest and widest sections.

5. Discussion and conclusions

As stated in the introduction, the main objective of this paper is to test the predictive capability of the theoretical model proposed in previous papers for the motion and transport of CSF in the subarachnoid space of the spinal canal [28,29]. The velocity field includes pulsating and steady components that were evaluated separately. The analytical model for the solute transport employs a two-time scale asymptotic procedure that effectively filters out the small cyclical variations of the solute concentration associated with the pulsating flow, so that the resulting evolution equation involves only the long-time scale, of interest in describing solute transport along distances comparable to the canal length. The predictions of the analytical model were compared with results of direct numerical simulations spanning 127 oscillatory cycles for two simplified, canonical geometries, namely, a canal of constant cross-section used previously in [28,29] and a modified geometry allowing for variations of the spinal-cord eccentricity along the canal, that being a typical feature of the human-body anatomy (see Fig. 1). For the latter, more complicated geometry, the time-averaged flow exhibits closed recirculating streamlines that dramatically affect the rate of solute transport. Although these recirculating Lagrangian vortices have been observed in recent subject-specific studies [27], more work, involving in-vitro and in-vivo experiments, is needed for a thorough characterization of their morphology.

The model predictions involve limited computational times that are about three orders of magnitude smaller than those required to generate the DNS results. The comparisons demonstrate that the time-averaged velocity field combined with the simple evolution Eq. (10) can provide sufficient accuracy to compute the drug dispersion in anatomically correct geometries, as needed to enable patient-specific predictions in ITDD applications. The capability of the theoretical model to describe the dispersion of a solute is particularly significant at high Schmidt numbers, typically found in drugs used in ITDD treatments, as Figs. 7 and 9 demonstrate. The agreement of the model with the numerical integrations of the complete momentum and species conservation equations indicates that the model correctly includes all of the relevant physical mechanisms acting in the long time scale, with solute transport being determined by the combined action of convection driven by the time-averaged Lagrangian velocity and transverse molecular diffusion across the canal.

Although the preliminary validation exercise presented above is restricted to two simplified canonical geometries, the model can be used in conjunction with realistic anatomical representations of the human spinal canal, as done in our

recent work [27]. Furthermore, despite the present model encompasses many of the essential physical mechanisms involved in the flow of CSF in the SSAS, there are additional important effects that should be considered in future work. For example, attention should be given to effects of extraventricular CSF production within the spinal canal [38,39] and pharmacokinetics phenomena, including drug enzymatic decay, tissue uptake, and clearance by the blood [20,40]. Consideration should also be given to the buoyancy-induced flow resulting from density differences between the drug and the CSF, which is known by clinicians to play an important role in the dispersion rate of ITDD drugs [41–45]. In addition, future extensions of the model should account for the presence of microanatomical features in the SSAS, such as trabeculae, nerve roots, and denticulate ligaments, which may have an important effect, as shown in previous numerical studies [46-48], leading to enhanced local mixing [23,25,49]. Previous modelling approaches include the work of Gupta et al. [47], who modelled the morphology of the complex trabecular structures as a porous medium with anisotropic permeability. Stockman [21,46] also investigated effects of nerve roots in computations with a rigid annular model including obstacles, showing that local flow stirring leads to effective diffusivities that are one order of magnitude larger than the molecular ones, which might have significant implications in the dispersion of a solute. Similar results were reported by Haga et al. [49], also considering a rigid model, in this case of the cervical region, with idealized nerve roots and denticulate ligaments. Additional studies have considered the complete SSAS, where the oscillatory CSF flow is driven by the periodic motion of the outer boundary, representing the dura [23,25,48]. In particular, Khani et al. [25] showed that the nerve roots modified the CSF dynamics, increasing the nonuniformity of the axial velocity and promoting steady-streaming, while the computations of Pahlavian et al. [48] and Tangen et al. (2015) [23] revealed that micro-anatomy-induced flow patterns promote the caudo-cranial spread of an intrathecally administered drug. Future studies should also address the potential effect of Taylor dispersion in the presence of obstacles, which has been recently assessed on the basis of a porous media model [50]. In addition, obstacles may induce secondary flows in the transverse plane, which, under certain conditions, can strongly enhance the Taylor dispersion mechanism, as described for the flow in a curved tube by [51]¹. More work is warranted to clarify how these local mixing flow events, occurring at the fast oscillatory time scale, contribute to the long-time drug transport and dispersion along the canal. These future refinements lie beyond the scope of the present contribution, which should be considered as a first but necessary step in the validation of an all-encompassing reduced-order model for the flow in the human spinal canal.

Acknowledgements

CGM and CMB acknowledge the support provided by the Spanish MINECO, Junta de Andalucía and European Funds through grants #DPI2017-88201-C3-2-R and #P18-FR-4619, respectively. The work of WC was supported by the 'Convenio Plurianual Comunidad de Madrid – Universidad Carlos III de Madrid' through grant CSFLOW-CM-UC3M, while that of JJL and ALS was supported by the National Science Foundation under grant #1853954. Support from the Red Nacional para el Desarrollo de la Microfluídica, RED2018102829T, is also acknowledged. We wish to dedicate this work to Professor J.C Lasheras who has recently passed away, just days before the publication of this manuscript.

Appendix A. Simplified description of the flow

As explained in [28], the solution for the flow in the asymptotic limit $\varepsilon \ll 1$ with $\alpha \sim 1$ and $k \sim 1$ can be obtained by using the doubly slender approximation $L \gg \ell_c \gg h_c$ in writing the conservation equations in simplified form and expressing the different variables as regular expansions

$$\begin{cases} u = u_{0} + \varepsilon u_{1} + \varepsilon^{2} u_{2} + \cdots \\ w = w_{0} + \varepsilon w_{1} + \varepsilon^{2} w_{2} + \cdots \\ v = v_{0} + \varepsilon v_{1} + \varepsilon^{2} v_{2} + \cdots \\ p' = p'_{0} + \varepsilon p'_{1} + \varepsilon^{2} p'_{2} + \cdots \\ \hat{p} = \hat{p}_{0} + \varepsilon \hat{p}_{1} + \varepsilon^{2} \hat{p}_{2} + \cdots \\ h' = h'_{0} + \varepsilon h'_{1} + \varepsilon^{2} h'_{2} + \cdots \end{cases}$$
(A.1)

Substituting these expressions into the equations and collecting terms with equal powers of ε leads to a succession of problems that can be solved sequentially.

A1. Leading-order oscillatory flow

At leading order the problem reduces to a linear time-dependent lubrication problem that can be solved to give the harmonic functions

$$u_0 = \operatorname{Re}(ie^{it}U), v_0 = \operatorname{Re}(ie^{it}V), w_0 = \operatorname{Re}(ie^{it}W),$$

¹ Note that for the unobstructed configuration under consideration here, the recirculating flow patterns in Fig. 8 could suggest that a similar mechanism could be at play, especially at large Schmidt numbers. However, differently from [51] where the characteristic length of the secondary flows is of the order of the tube diameter, in the present case the size of the recirculating flow is of the order of the length of the canal, with a characteristic time for a fluid particle to traverse the secondary flow that is much larger than the period of the cycle. Thus, it is unlikely that this mechanism plays a relevant role in the current situation, as inferred by the similar evolution of the axial solute concentration distributions, $[\int_0^1 (\bar{h} \int_0^1 c_0 d\eta) ds]$, obtained numerically for the two Schmidt numbers shown in Figs. 9(a) and (b) (solid curves on the side plots).

$$p'_0 = \operatorname{Re}(e^{it}P), \, \hat{p}_0 = \operatorname{Re}(e^{it}\hat{P}), \, h'_0 = \operatorname{Re}(e^{it}H), \tag{A.2}$$

involving the complex functions $U(x, s, \eta)$, $W(x, s, \eta)$, $V(x, s, \eta)$, P(x), $\hat{P}(x, s)$, and H(x). The complex velocities are expressed in terms of the components of the pressure gradient

$$U = \frac{\mathrm{d}P}{\mathrm{d}x}G, \quad W = \frac{1}{\ell}\frac{\partial \hat{P}}{\partial s}G,\tag{A.3}$$

and

$$V = -\frac{1}{\ell} \frac{\partial}{\partial x} \left(\ell \frac{dP}{dx} \bar{h} \int_0^{\eta} G d\eta \right) - \frac{1}{\ell} \frac{\partial}{\partial s} \left(\frac{1}{\ell} \frac{\partial \hat{P}}{\partial s} \bar{h} \int_0^{\eta} G d\eta \right) + \frac{\partial \bar{h}}{\partial x} \frac{dP}{dx} \eta G + \frac{1}{\ell} \frac{\partial \bar{h}}{\partial s} \frac{1}{\ell} \frac{\partial \hat{P}}{\partial s} \eta G. \tag{A.4}$$

with

$$G(x, \eta, s) = 1 - \frac{\cosh\left[\frac{\alpha \bar{h}}{2} \frac{1+i}{\sqrt{2}} (2\eta - 1)\right]}{\cosh\left[\frac{\alpha \bar{h}}{2} \frac{1+i}{\sqrt{2}}\right]}.$$
(A.5)

As explained in the main text, the displacement H(x) is obtained by solving the boundary-value problem (7). Finally, the azimuthal pressure gradient is given in terms of the displacement by

$$\frac{1}{\ell} \frac{\partial \hat{P}}{\partial s} = -\frac{1}{q} \left\{ \frac{\partial}{\partial x} \left[\frac{\ell}{k^2} \left(\int_0^s q d\tilde{s} \right) \frac{dH}{dx} \right] + s\ell H \right\},\tag{A.6}$$

where q(s, x) is defined in (8), to be used together with

$$\frac{\mathrm{d}P}{\mathrm{d}x} = \frac{1}{k^2} \frac{\mathrm{d}H}{\mathrm{d}x},\tag{A.7}$$

in evaluating the velocity from (A.3) and (A.4).

A2. Steady streaming

The above harmonic velocity has a zero average value, i.e. $(\langle u_0 \rangle, \langle w_0 \rangle, \langle v_0 \rangle) = (0, 0, 0)$ with $\langle \cdot \rangle = \frac{1}{2\pi} \int_0^{2\pi} \cdot dt = 0$. As shown previously by [28], the first-order corrections (u_1, w_1, v_1) , arising from the nonlinear effects associated with convective acceleration and canal deformation, contain a steady component $(u_{SS}, v_{SS}, w_{SS}) = (\langle u_1 \rangle, \langle v_1 \rangle, \langle w_1 \rangle)$. This so-called steady-streaming velocity can be evaluated from

$$(u_{SS}, v_{SS}, w_{SS}) = \frac{1}{2} \operatorname{Re}(\mathcal{U}_{SS}, \mathcal{V}_{SS}, \mathcal{W}_{SS}),$$
 (A.8)

involving the complex functions

$$\begin{split} \frac{\mathcal{U}_{SS}}{\bar{h}^{2}\alpha^{2}} &= -\left(\frac{\mathrm{d}\mathcal{P}_{1}'}{\mathrm{d}x}\right) \frac{(1-\eta)\eta}{2} + \eta \int_{0}^{\eta} \mathcal{F}_{x} \mathrm{d}\bar{\eta} - \int_{0}^{\eta} \mathcal{F}_{x} \bar{\eta} \mathrm{d}\bar{\eta} - \eta \int_{0}^{1} \mathcal{F}_{x} (1-\eta) \mathrm{d}\eta \\ \frac{\mathcal{W}_{SS}}{\bar{h}^{2}\alpha^{2}} &= -\left(\frac{1}{\ell} \frac{\partial \hat{\mathcal{P}}_{1}}{\partial s}\right) \frac{(1-\eta)\eta}{2} + \eta \int_{0}^{\eta} \mathcal{F}_{s} \mathrm{d}\bar{\eta} - \int_{0}^{\eta} \mathcal{F}_{s} \bar{\eta} \mathrm{d}\bar{\eta} - \eta \int_{0}^{1} \mathcal{F}_{s} (1-\eta) \mathrm{d}\eta \\ \mathcal{V}_{SS} &= -\frac{1}{\ell} \frac{\partial}{\partial x} \left[\ell \int_{0}^{\eta} \left(\bar{h}\mathcal{U}_{SS} + \mathrm{i}H^{*}U\right) \mathrm{d}\eta\right] + \eta \frac{\partial \bar{h}}{\partial x} \mathcal{U}_{SS} + \mathrm{i}\eta \frac{\partial H^{*}}{\partial x} U \\ &- \frac{1}{\ell} \frac{\partial}{\partial s} \left[\int_{0}^{\eta} \left(\bar{h}\mathcal{W}_{SS} + \mathrm{i}H^{*}W\right) \mathrm{d}\eta\right] + \eta \frac{1}{\ell} \frac{\partial \bar{h}}{\partial s} \mathcal{W}_{SS} + \mathrm{i}\eta \frac{1}{\ell} \frac{\partial H^{*}}{\partial s} W, \end{split} \tag{A.9}$$

with

$$\mathcal{F}_{x} = \frac{1}{\ell} \frac{\partial}{\partial x} (\ell U U^{*}) + \frac{1}{\bar{h}} \frac{\partial}{\partial \eta} (U V^{*}) + \frac{1}{\ell} \frac{\partial}{\partial s} (U W^{*}) - \frac{\eta}{\bar{h}} \frac{\partial}{\partial \eta} (U H^{*})$$

$$- \frac{\partial \bar{h}}{\partial x} \frac{\eta}{\bar{h}} \frac{\partial}{\partial \eta} (U U^{*}) - \frac{1}{\ell} \frac{\partial \bar{h}}{\partial s} \frac{\eta}{\bar{h}} \frac{\partial}{\partial \eta} (U W^{*}) + \frac{2}{\bar{h}^{3} \alpha^{2}} \frac{\partial^{2}}{\partial \eta^{2}} (i U H^{*})$$
(A.10)

and

$$\mathcal{F}_{s} = \frac{\partial}{\partial x}(WU^{*}) + 2\frac{(WU^{*})}{\ell}\frac{\partial\ell}{\partial x} + \frac{1}{\bar{h}}\frac{\partial}{\partial\eta}(WV^{*}) + \frac{1}{\ell}\frac{\partial}{\partial s}(WW^{*}) - \frac{\eta}{\bar{h}}\frac{\partial}{\partial\eta}(WH^{*}) - \frac{\partial\bar{h}}{\bar{h}}\frac{\eta}{\partial\eta}\frac{\partial}{\partial\eta}(WU^{*}) - \frac{1}{\ell}\frac{\partial\bar{h}}{\partial s}\frac{\eta}{\bar{h}}\frac{\partial}{\partial\eta}(WW^{*}) + \frac{2}{\bar{h}^{3}\alpha^{2}}\frac{\partial^{2}}{\partial\eta^{2}}(iWH^{*}).$$
(A.11)

where the asterisk * denotes here complex conjugates, and the auxiliary pressure-gradient functions are determined by imposing the continuity constraints

$$\int_{0}^{1} \bar{h} \left(\int_{0}^{1} \mathcal{U}_{SS} d\eta \right) ds + i \int_{0}^{1} H^{*} \int_{0}^{1} U d\eta ds = 0, \tag{A.12}$$

and

$$\bar{h} \int_0^1 \mathcal{W}_{SS} d\eta + iH^* \int_0^1 W d\eta = -\frac{\partial}{\partial x} \left[\ell \int_0^s \left(\bar{h} \int_0^1 \mathcal{U}_{SS} d\eta + iH^* \int_0^1 U d\eta \right) ds \right]. \tag{A.13}$$

A3. Stokes drift

As shown by [29], the Lagrangian velocity components are computed according to $u_L = u_{SS} + u_{SD}$, $v_L = v_{SD} + v_{SD}$, and $w_L = w_{SD} + w_{SD}$, where the Stokes-drift velocities are given by

$$(u_{SD}, v_{SD}, w_{SD}) = \frac{1}{2} \operatorname{Re}[i (\mathcal{U}_{SD}, \mathcal{V}_{SD}, \mathcal{W}_{SD})], \tag{A.14}$$

where

$$\mathcal{U}_{SD} = \frac{1}{\bar{h}} \left[UH^* + \frac{1}{\ell} \frac{\partial}{\partial s} (\bar{h}UW^*) \right] + \frac{1}{\bar{h}} \frac{\partial}{\partial \eta} \left\{ U \left[V^* - \eta \left(H^* + \frac{1}{\ell} \frac{\partial \bar{h}}{\partial s} W^* \right) \right] \right\},
\mathcal{V}_{SD} = \frac{1}{\ell} \frac{\partial}{\partial x} (\ell V U^*) + \frac{1}{\ell} \frac{\partial}{\partial s} (VW^*) - \frac{\eta}{\bar{h}} \frac{\partial}{\partial \eta} \left[V \left(H^* + \frac{\partial \bar{h}}{\partial x} U^* + \frac{1}{\ell} \frac{\partial \bar{h}}{\partial s} W^* \right) \right],
\mathcal{W}_{SD} = \frac{1}{\bar{h}} \left[WH^* + \frac{\partial}{\partial x} (\bar{h}WU^*) \right] + \frac{1}{\bar{h}} \frac{\partial}{\partial \eta} \left\{ W \left[V^* - \eta \left(H^* + \frac{\partial \bar{h}}{\partial x} U^* \right) \right] \right\}.$$
(A.15)

Supplementary material

Supplementary material associated with this article can be found, in the online version, at doi:10.1016/j.apm.2021.01.037.

References

- [1] A.A. Linninger, K. Tangen, C.-Y. Hsu, D. Frim, Cerebrospinal fluid mechanics and its coupling to cerebrovascular dynamics, Annu. Rev. Fluid Mech. 48 (1) (2016) 219–257.
- [2] M. Klarica, M. Radoš, D. Orešković, The movement of cerebrospinal fluid and its relationship with substances behavior in cerebrospinal and interstitial fluid, Neuroscience 414 (2019) 28–48.
- [3] G. Ringstad, L.M. Valnes, A.M. Dale, A.H. Pripp, S.S. Vatnehol, K.E. Emblem, K.A. Mardal, P.K. Eide, Brain-wide glymphatic enhancement and clearance in humans assessed with mri, JCI Insight 3 (13) (2018) e121537.
- [4] N.A. Jessen, A.S. Munk, I. Lundgaard, M. Nedergaard, The glymphatic system: a beginner's guide, Neurochem Res. 40 (12) (2015) 25832599.
- [5] A.C. Bunck, J.R. Kroeger, A. Juettner, A. Brentrup, B. Fiedler, G.R. Crelier, B.A. Martin, W. Heindel, D. Maintz, W. Schwindt, et al., Magnetic resonance 4D flow analysis of cerebrospinal fluid dynamics in Chiari I malformation with and without syringomyelia, Eur. Radiol. 22 (9) (2012) 1860–1870.
- [6] S.H. Pahlavian, F. Loth, M. Luciano, J. Oshinski, B.A. Martin, Neural tissue motion impacts cerebrospinal fluid dynamics at the cervical medullary junction: a patient-specific moving-boundary computational model, Ann. Biomed. Eng. 43 (12) (2015) 2911–2923.
- [7] J.M. Rice-Edwards, A pathological study of syringomyelia, J. Neurol. Neurosurg. Psychiatry 40 (1977) 198.
- [8] B.A. Martin, R. Labuda, T.J. Royston, J.N. Oshinski, B. Iskandar, F. Loth, Spinal subarachnoid space pressure measurements in an in vitro spinal stenosis model: implications on syringomyelia theories, J. Biomech. Eng. 132 (11) (2010) 111007.
- [9] J. Yeo, S. Cheng, S. Hemley, B. Lee, M. Stoodley, L. Bilston, Characteristics of csf velocity-time profile in posttraumatic syringomyelia, Am. J. Neuroradiol. 38 (9) (2017) 1839–1844.
- [10] V. Vinje, J. Brucker, M.E. Rognes, K.A. Mardal, V. Haughton, Fluid dynamics in syringomyelia cavities: effects of heart rate, CSF velocity, CSF velocity waveform and craniovertebral decompression, Neuroradiol J. 35 (5) (2018) 482–489.
- [11] B.M. Onofrio, T.L. Yaksh, P.G. Arnold, Continuous low-dose intrathecal morphine administration in the treatment of chronic pain of malignant origin, Mayo Clin. Proc. 56 (1981) 516520.
- [12] L. Lynch, Intrathecal drug delivery systems, Contin. Educ. Anaesth. Crit. Care Pain 14 (2014) 2731.
- [13] M.J. Fowler, J.D. Cotter, B.E. Knight, E.M. Sevick-Muraca, D.I. Sandberg, R.W. Sirianni, Intrathecal drug delivery in the era of nanomedicine, Adv. Drug. Deliv. Rev. (2020) Inpress.
- [14] Y.C. Lee, C.C. Hsieh, J.P. Chuang, C.Y. Li, The necessity of intrathecal chemotherapy for the treatment of breast cancer patients with leptomeningeal metastasis: a systematic review and pooled analysis, Curr. Probl. Cancer 41 (2017) 355370.
- [15] F. Remeš, R. Tomaš, V. Jindrák, V. Vaniš, M. Setlík, Intraventricular and lumbar intrathecal administration of antibiotics in postneurosurgical patients with meningitis and/or ventriculitis in a serious clinical state, J. Neurosurg. 119 (2013) 15961602.
- [16] M.M. Bottros, P.J. Christo, Current perspectives on intrathecal drug delivery, J. Pain Res. 7 (2014) 615626.
- [17] K. Tangen, J. Sullivan, R.W. Holt, I. Nestorov, A. Verma, A.A. Linninger, In-vivo intrathecal tracer dispersion in cynomolgus monkey validates wide biodistribution along neuraxis, IEEE Trans. Biomed. Eng. 67 (4) (2020) 1122–1132, doi:10.1109/TBME.2019.2930451.
- [18] C.M. Bernards, Cerebrospinal fluid and spinal cord distribution of baclofen and bupivacaine during slow intrathecal infusion in pigs., Anesthesiology 105 (2006) 169178.
- [19] H.D. Hettiarachchi, Y. Hsu, T.J. Harris Jr., R. Penn, A.A. Linninger, The effect of pulsatile flow on intrathecal drug delivery in the spinal canal, Ann. Biomed. Eng. 39 (10) (2011) 25922602.
- [20] K.M. Tangen, R. Leval, A.I. Mehta, A.A. Linninger, Computational and in vitro experimental investigation of intrathecal drug distribution: parametric study of the effect of injection volume, cerebrospinal fluid pulsatility, and drug uptake, Anesthesia & Analgesia 124 (2017) 1686–1696.
- [21] H.W. Stockman, Effect of anatomical fine structure on the dispersion of solutes in the spinal subarachnoid space, J. Biomech. Eng. 129 (5) (2007) 666675.

- [22] Y. Hsu, H.D. Hettiarachchi, D.C. Zhu, A.A. Linninger, The frequency and magnitude of cerebrospinal fluid pulsations influence intrathecal drug distribution: key factors for interpatient variability, Anesth. Analg. 115 (2) (2012) 386–394.
- [23] K.M. Tangen, Y. Hsu, D.C. Zhu, A.A. Linninger, CNS wide simulation of flow resistance and drug transport due to spinal microanatomy, J. Biomech. 48 (10) (2015) 2144–2154.
- [24] M. Khani, T. Xing, C. Gibbs, J.N. Oshinski, G.R. Stewart, J.R. Zeller, B.A. Martin, Nonuniform moving boundary method for computational fluid dynamics simulation of intrathecal cerebrospinal flow distribution in a cynomolgus monkey, J Biomech Eng. 139 (8) (2017) 0810051–08100512.
- [25] M. Khani, L.R. Sass, T. Xing, M.K. Sharp, O. Balédent, B.A. Martin, Anthropomorphic model of intrathecal cerebrospinal fluid dynamics within the spinal subarachnoid space: spinal cord nerve roots increase steady-Streaming, J. Biomech. Eng. 140 (8) (2018) 081012.
- [26] V. Haughton, K.-A. Mardal, Spinal fluid biomechanics and imaging: an update for neuroradiologists, Am. J. Neuroradiol. 35 (10) (2014) 1864-1869.
- [27] W. Coenen, C. Gutiérrez-Montes, S. Sincomb, E. Criado-Hidalgo, K. Wei, K. King, V. Haughton, C. Martínez-Bazán, A.L. Sánchez, J.C. Lasheras, Subject-specific studies of CSF bulk flow patterns in the spinal canal: implications for the dispersion of solute particles in intrathecal drug delivery, Am. J. Neuroradiol. 40 (7) (2019) 1242–1249.
- [28] A.L. Sánchez, C. Martínez-Bazán, C. Gutiérrez-Montes, E. Criado-Hidalgo, G. Pawlak, W. Bradley, V. Haughton, J.C. Lasheras, On the bulk motion of the cerebrospinal fluid in the spinal canal, J. Fluid Mech. 841 (2018) 203–227.
- [29] J.J. Lawrence, W. Coenen, A.L. Sánchez, G. Pawlak, C. Martínez-Bazán, V. Haughton, J.C. Lasheras, On the dispersion of a drug delivered intrathecally in the spinal canal, J. Fluid Mech. 861 (2019) 679–720.
- [30] M.A. Reina, J.A. De Andrés, A. Hadzic, A. Prats-Galino, X. Sala-Blanch, A.A.J. van Zundert, Atlas of functional anatomy for regional anesthesia and pain medicine: Human structure, ultrastructure and 3D reconstruction images, Springer, 2015.
- [31] F. Loth, M.A. Yardimci, N. Alperin, Hydrodynamic modeling of cerebrospinal fluid motion within the spinal cavity, ASME J. Biomech. Eng. 123 (1) (2001) 7179.
- [32] L.R. Sass, M. Khani, G.C. Natividad, R.S. Tubbs, O. Baledent, B.A. Martin, A 3d subject-specific model of the spinal subarachnoid space with anatomically realistic ventral and dorsal spinal cord nerve rootlets, Fluids Barriers CNS 14 (1) (2017) 36.
- [33] W. Kalata, B.A. Martin, J.N. Oshinski, M. Jerosch-Herold, T.J. Royston, F. Loth, MR measurement of cerebrospinal fluid velocity wave speed in the spinal canal, IEEE Trans. Biomed. Eng. 56 (6) (2009) 1765–1768.
- [34] B. Sweetman, A.A. Linninger, Cerebrospinal fluid flow dynamics in the central nervous system, Ann. Biomed. Eng. 39 (2011) 484-496.
- [35] R.I. Issa, Solution of the implicitly discretised fluid flow equations by operator-splitting, J. Comput. Phys. 62 (1) (1986) 40-65.
- [36] J. Tao, Q. Sun, W. Liang, Z. Chen, Y. He, M. Dehmer, Computational fluid dynamics based dynamic modeling of parafoil system, Appl. Math. Modell. 54 (2018) 136–150.
- [37] R.J. Bert, S.M. Hayek, T.L. Yaksh, Modeling spinal intrathecal drug distribution: the challenge of defining and predicting cerebrospinal fluid dynamics, Anesthesia & Analgesia 124 (2017) 1403–1406.
- [38] S. Yamada, Cerebrospinal fluid physiology: visualization of cerebrospinal fluid dynamics using the magnetic resonance imaging time-spatial inversion pulse method, Croat Med J 55 (4) (2014) 337346.
- [39] E.K. Lindstrøm, G. Ringstad, K.A. Mardal, P.K. Eide, Cerebrospinal fluid volumetric net flow rate and direction in idiopathic normal pressure hydrocephalus, Neuroimage Clin. 20 (2018) 731–741.
- [40] G. Pizzichelli, Modelling approaches of innovative drug delivery strategies for the Central Nervous System, Scuola Superiore Sant'Anna, 2016 Ph.D. thesis.
- [41] J.A.W. Wildsmith, J.H. McClure, D.T. Brown, D.B. Scott, Effects of posture on the spread of isobaric and hyperbaric amethocaine, Br. J. Anaesth. 53 (3) (1981) 273–278.
- [42] R.W.D. Mitchell, G.M.R. Bowler, D.B. Scott, H.H. Edström, Effects of posture and baricity on spinal anaesthesia with 0.5% bupivacaine 5 ml, Br J Anaesth 61 (2) (1988) 139–143.
- [43] H.M.R. Povey, J. Jacobsen, J. Westergaard-Nielsen, Subarachnoid analgesia with hyperbaric 0.5% bupivacaine: effect of a 60-min period of sitting, Acta Anaesthesiol Scand 33 (4) (1989) 295–297.
- [44] M.G. Richardson, R. Thakur, J.S. Abramowicz, R.N. Wissler, Maternal posture influences the extent of sensory block produced by intrathecal dextrose-free bupivacaine with fentanyl for labor analgesia, Anesth. Analg. 83 (6) (1996) 1229–1233.
- [45] B.T. Veering, T.T.M. Immink-Speet, A.G.L. Burm, R. Stienstra, J.W. van Kleef, Spinal anaesthesia with 0.5% hyperbaric bupivacaine in elderly patients: effects of duration spent in the sitting position, Br J Anaesth 87 (5) (2001) 738–742.
- [46] H.W. Stockman, Effect of anatomical fine structure on the flow of cerebrospinal fluid in the spinal subarachnoid space, J. Biomech. Eng. 128 (1) (2006) 106–114.
- [47] S. Gupta, M. Soellinger, P. Boesiger, D. Poulikakos, V. Kurtcuoglu, Three-dimensional computational modeling of subject-specific cerebrospinal fluid flow in the subarachnoid space, J. Biomech. Eng. 131 (2) (2009) 021010.
- [48] S.H. Pahlavian, T. Yiallourou, R.S. Tubbs, A.C. Bunck, F. Loth, M. Goodin, M. Raisee, B.A. Martin, The impact of spinal cord nerve roots and denticulate ligaments on cerebrospinal fluid dynamics in the cervical spine, PLoS ONE 9 (4) (2014) e91888.
- [49] P.T. Haga, G. Pizzichelli, M. Mortensen, M. Kuchta, S.H. Pahlavian, E. Sinibaldi, B.A. Martin, K.A. Mardal, A numerical investigation of intrathecal isobaric drug dispersion within the cervical subarachnoid space, PLoS ONE 12 (3) (2017) e0173680.
- [50] M.K. Sharp, R.O. Carare, B.A. Martin, Dispersion in porous media in oscillatory flow between flat plates: applications to intrathecal, periarterial and paraarterial solute transport in the central nervous system, Fluids Barriers CNS 16 (13) (2019).
- [51] M.K. Sharp, R.D. Kamm, A.H. Shapiro, E. Kimmel, G.E. Karniadakis, Dispersion in a curved tube during oscillatory flow, J. Fluid Mech. 223 (1991) 537–563.